

A DNS Study of entrainment in an axisymmetric turbulent jet as an episodic process

Prasanth Prabhakaran*

*Max Planck Institute for Dynamics and Self-Organization, Goettingen, 37077, Germany
Engineering Mechanics Unit, Jawaharlal Nehru Center for Advanced Scientific Research, Bangalore 560064, India*

Sachin Y. Shinde†

*Department of Mechanical Engineering, Indian Institute of Technology, Kanpur, 208016,, India
Engineering Mechanics Unit, Jawaharlal Nehru Center for Advanced Scientific Research, Bangalore 560064, India*

Roddam Narasimha‡

*Engineering Mechanics Unit, Jawaharlal Nehru Center for Advanced Scientific Research, Bangalore 560064, India
(Dated: February 1, 2022)*

This investigation is based on a Direct Numerical Simulation (DNS) of a steady self-preserving incompressible axisymmetric turbulent jet at a Reynolds number of 2400 (based on orifice diameter d_0 and mean exit velocity \bar{w}_0 at floor level $z = 0$). The DNS data enable accurate maps of the outer irrotational flow field, and also the vorticity field $\boldsymbol{\omega}(\mathbf{x}, t)$ in the turbulent core of the jet. It is found necessary to define two separate boundaries of the jet. The first is an inner boundary (turbulent/nonturbulent, T/NT) at $|\boldsymbol{\omega}(\mathbf{x}, t)| = 0.5$ (quoted in units of local center-line velocity and half-width), from where $|\boldsymbol{\omega}(\mathbf{x}, t)|$ rises steeply towards the turbulent core whose boundary is located around $|\boldsymbol{\omega}(\mathbf{x}, t)| = 1.0$. The second is an outer rotational/irrotational (R/IR) boundary at $|\boldsymbol{\omega}(\mathbf{x}, t)| = 0.1$, beyond which the flow may be considered irrotational. In the diametral and axial sections, the separation between the inner and outer boundaries can vary from 2η to 5λ (η and λ are the Kolmogorov and Taylor length scales respectively). In the latter case, $|\boldsymbol{\omega}(\mathbf{x}, t)| > 0.1$ between the two boundaries but is not stochastic, so the inter-boundary region is in the nature of a viscous laminar sheath. This region can often be traced to a fossil of a vortical tongue that has a long life of the order of a few hundred flow units (d_0/\bar{w}_0), because of the very low advective velocity towards the edge of the jet. The velocity field beyond the outer boundary often has ordered, nearly irrotational circulatory motions. These can be shown, in simpler cases, to be the velocity field induced by one or more vorticity elements in a coherent structure in the turbulent core. A detailed examination of axial and diametral sections indicates that there are periods when there is a large inrush of ambient fluid into parts of the T/NT interface, which gets distorted into a gulf or ‘well’ that can be both twisted and deep. Sections of these wells often appear as what may be called as ‘lakes’ of irrotational fluid in diametral sections of the jet flow. Part of the inrushing fluid crosses the T/NT interface within the well and is entrained into the turbulent core, by a process that can legitimately be called nibbling. The duration of such an inrush process can be of the order up to 20 flow units and suggests that entrainment can be an episodic process in which an inrush event accelerates ambient fluid even as it is pushed into a narrowing gulf, where it penetrates the T/NT interface of the gulf by nibbling. This supports the view that engulfment and nibbling are successive stages in the life of an entrainment episode. In view of the well-known difficulties associated with the analysis of fluid flow past a highly convoluted 3D fractal interface, the flow is analyzed here by the device of enclosing the jet in $z_1 \leq z \leq z_2$ by a minimal cylindrical disk of height $z_2 - z_1$ and radius nearly touching the radially farthest point on the inner edge of the jet anywhere within the disk. By analyzing the radial flow at the edge of the disk with flow at the T/NT interface in the same angular sector, it is found that the two flows are correlated in about 90% of the time and anti-correlated the rest of the time. A mass flux budget across the surfaces of the disk and the turbulent core of the jet enables determination of the inrush events around the polar angle in the diametral section, and suggest an average of 12 to 16 events in 360° . This episodic view permits the introduction of such flow parameters as burstiness, which is a measure of the compactness and intensity of the events under study, as used in the analysis of momentum flux events in the atmospheric boundary layer [1]. In the present case, similar episodes are responsible for entrainment. In the turbulent round jet, the entrainment burstiness is found to be of order 0.75, comparable to the momentum flux burstiness found in a turbulent boundary layer.

PACS numbers: 47.32.ck, 47.63.M-, 47.27.wg

* prasantp@mtu.edu - presently at Michigan Technological University

† sachin@iitk.ac.in

‡ roddam@jncasr.ac.in

I. INTRODUCTION

The process by which ambient fluid is entrained into a turbulent shear flow has been a question of great importance for a long time. The first significant study of the problem, due to Corrsin (1955) [2], was inspired by a striking instantaneous shadowgraph of the turbulent wake of a bullet traveling at supersonic speeds. This picture showed a sharp boundary between the turbulent core of the wake and the ambient fluid. Corrsin proposed that entrainment occurred due to what has come to be called the ‘nibbling’ of the ambient fluid at the turbulent / non-turbulent (T/NT) interface of the flow across a viscous super-layer whose thickness scales with the Kolmogorov length. On the other hand, the work of Brown & Roshko (1972, 1974) [3, 4] presented striking optical visualizations of flow in turbulent free-shear (or mixing) layers showing highly organized structures, and concluded that entrainment occurred by ‘engulfment’ of ambient fluid through the velocity induced by the coherent structures present in the turbulent core flow. Studies by Dimotakis (1983) [5] on an axisymmetric jet showed that the instantaneous boundary of the turbulent core (as marked by passive scalar dye concentration) was highly convoluted, and supported the idea for a dominant role of coherent structures in entrainment, by engulfment of ambient fluid.

The main issue in much recent work on entrainment in turbulent shear flows can be summarized as a debate on nibbling vs. engulfment as primary candidates for the entrainment mechanism. While it is realized that it is not easy to make a precise distinction between the two (Da Silva (2014) [6]), recent work, conceding that engulfment may be responsible for most of the entrainment in mixing layers (Westerweel *et al.* (2002) [7]), has generally concluded that it accounts for little in other turbulent flows like jets, wakes (Bisset *et al.* (2002) [8]) and grid turbulence (Holzner & Luethi (2011) [9]). A related part of the debate has been concerned with determining the length and velocity scales relevant to the entrainment process, and in particular the roles played by the Kolmogorov and Taylor length scales therein [6, 10, 11].

On these issues the jet has been the most widely studied turbulent shear flow (experiments on round jets reported by Westerweel *et al.* (2002) [7], Wolf *et al.* (2012) [12]; DNS results on a temporal round jet by Mathew & Basu (2002) [13], on a temporally evolving plane jet by Reeuwijk and Holzner (2014) [14] and on a spatially developing plane jet by Da Silva (2010) [11]). The analysis of Mathew & Basu [13] concludes that most of the entrainment occurs due to small-scale action at the T/NT interface. This idea was further supported by Westerweel *et al.* (2005, 2009) [10, 15] and Wolf *et al.* (2012) [12] based on PIV measurements on a round jet. All these studies report that small-scale activity at the T/NT interface plays a dominant role in the entrainment process. Westerweel *et al.* (2009) [10] concluded that large scale engulfment contributed about 8% of the net mass flux. Wolf *et al.* (2012) [12] used particle tracking velocimetry to generate the 3D velocity field and compute the interface velocity using this data. Their studies suggested that the entrainment velocity is dominated by viscous action due to the small scale eddies at the T/NT interface. They also show that the entrainment velocity is strongly influenced by the local curvature of the interface with higher entrainment at the concave region of the T/NT interface. The analysis on the DNS of temporal jets by Reeuwijk & Holzner (2014) [14] shows the presence of a viscous super layer (VSL) enveloping the vortical core. They also define a buffer region similar to those in wall bounded flows, which connects the VSL with the turbulent core.

Philip and Marusic (2012) [16] proposed a large eddy model to reproduce some of the features of the large scale motion in jets and wakes. Recent work by Mistry *et al.* (2016) [17], using simultaneous PIV and PLIF measurements, stresses the multi-scale nature of the entrainment velocity and the scale-independence of mass flux in a turbulent jet. These studies, along with the work of Turner (1986) [18], Dahm & Dimotakis (1987) [19], Mathew & Basu (2002), Wolf *et al.* (2012) [12] and Reeuwijk & Holzner (2014) [14] propose that entrainment dynamics is dictated or imposed by large-scale coherent motions, to which small scale viscous action adjusts itself to maintain a scale-independent mass flux rate.

In a recent work Burrridge *et al.* (2017) [20] have reported simultaneous PIV/PLIF measurements on the entrainment dynamics in a turbulent axisymmetric plume. They present conditional statistics highlighting the role of large scale motions in the entrainment process. Their studies suggest that significant momentum is imparted to the fluid outside the T/NT interface in the zones between the coherent structures. Moreover, they conclude that turbulent entrainment in a plume is dominated by engulfment in the first stage followed by viscous nibbling. Similar conclusions on the role of the large scale motions were reported earlier by Plourde *et al.* (2008) [21]. They associate the presence of large scale organized motions with higher instantaneous entrainment levels.

To the best of our knowledge there has been no numerical study of the round jet from the entrainment point of view, and the present work was undertaken in part to fill this gap. The big advantages of having DNS data are that the vorticity vector field can be accurately determined, enabling a vorticity view of the T/NT interface, and the flow field in the ambient fluid beyond the edge of the jet can be accurately determined. The present report starts by presenting, as a first step, a physical picture of entrainment largely derived from DNS imagery. This is followed by an analysis of the entrainment budget across a cylindrical disc of finite thickness circumscribing the jet in the self-preserving zone of the jet. The analysis strongly suggests an episodic (spatially discrete and temporally intermittent) nature of the

entrainment process. One reason for this approach is that while much attention has been given in earlier studies to flow within and very close to the fully turbulent core, surprisingly little attention has been given to the structure of the flow in the ambient fluid outside the turbulent core in a slightly more extended neighborhood (over an area with a length scale of order b_w , the radius of the jet at half the mean center-line velocity). This may partly be due to difficulties in making accurate measurements of the very low velocities in the ambient fluid. Furthermore, early models for what may be called the ‘ambient near-field’ visualized it as resulting from a distribution of sinks along the center-line of the jet (Phillips (1955) [22], Bradshaw (1976) [23]), but this approach does not throw any light on the spatio-temporal structure of the flow in the ambient fluid. A very useful recent review of these developments has been presented by Da Silva *et al.* (2014) [6].

Several definitions of entrainment have been proposed in the literature (Turner (1986) [18]). All the experiments and simulations on jets and wakes discussed so far define entrainment as the velocity at which the turbulent flow spreads into the irrotational ambient. Here we define entrainment as the rate at which the irrotational ambient fluid enters into the vortical turbulent core of the jet. The two definitions have significantly different implications which are best understood by looking at a planar wake. According to the former definition of entrainment, a planar wake has non-zero entrainment as the wake spreads in the streamwise direction. On the contrary, the wake has a net zero entrainment using the latter definition as the average mass flux in the streamwise direction is a constant. It is important to distinguish between encroachment (as in the spreading wake with no change in mass flux) and entrainment (which involves an increase in turbulent mass flux). In a turbulent round jet, the net mass flux in the streamwise direction as well as the diameter increases downstream. We investigate here the entrainment dynamics close to the T/NT interface in a turbulent round jet.

Against this background we present data on the instantaneous flow field outside the turbulent core in a round jet, as obtained by a direct numerical simulation of the jet flow. This makes it possible to visualize the general structure of the ambient flow field, and examine its possible relation to the vorticity field (or other flow characteristics) within the jet. A general schematic view of the velocity field, as sketched for example by Philip & Marusic (2012) [16], implies that the ambient fluid flows into the turbulent jet along more or less parallel streamlines almost right up to the T/NT interface, where it is entrained into the jet core across its edge. A somewhat more structured velocity field is indicated by the measurements reported by Westerweel *et al.* (2009) [10] (Figs. 19 and 20). Here we present evidence, chiefly through flow imagery, indicating that the instantaneous flow in the ambient neighborhood of the turbulent edge of the jet is much more organized than thought previously, and the entrainment across the T/NT interface is episodic in nature. A more detailed quantitative study will appear separately.

The paper is organized into ten sections. We start with the description of the numerical procedure used for the simulation and the details on the accuracy of the data, followed by a discussion on the identification of the boundaries separating the turbulent core from the (nearly) irrotational ambient. Later, the axial and diametral sections are analysed to understand the dynamics near the T/NT interface. Based on these details we conduct a quantitative analysis of the mass flux near the T/NT interface followed by concluding remarks.

II. SIMULATION DETAILS

Fig. 1 shows a schematic of an axial section of the jet, where d_0 represents the orifice diameter from which the jet issues with a top hat velocity profile characterized by a uniform jet exit mean velocity \bar{w}_0 . The flow is governed by the incompressible Navier-Stokes equations (in non-dimensional form with jet exit velocity scale \bar{w}_0 and nozzle exit diameter d_0 as velocity and length scales respectively),

$$\nabla \cdot \mathbf{u} = 0, \quad (1)$$

$$(\partial \mathbf{u} / \partial t) + (\mathbf{u} \cdot \nabla) \mathbf{u} = -\nabla p + (1/Re) \nabla^2 \mathbf{u}, \quad (2)$$

where \mathbf{u} , p represent the flow velocity vector and pressure respectively, and $Re = \bar{w}_0 d_0 / \nu$ is the Reynolds number ($= 2400$ in the present simulations). Unless otherwise specified, all distances, velocities and time presented here are non-dimensionalized with d_0 and w_0 as scales, and vorticity with the time-mean local scales at height z , *viz.*, centerline velocity $\bar{w}_c(z)$ and half-velocity jet width $b_w(z)$. Also note that, unless otherwise stated, all flow variables are non-dimensional.

The equations are solved using the extension of Harlow & Welsh’s scheme [24] to non-uniform grids as proposed by Verstappen & Veldman (2003) [25], using a second-order finite volume framework. The governing equations are integrated in time using the second-order Adams-Bashforth scheme with a time step $\Delta t = 0.005$. A non-uniform Cartesian mesh is used to resolve all the relevant scales in the turbulent part of the flow-field. The velocity and pressure variables are stored in a staggered arrangement to prevent pressure-velocity decoupling. The pressure variable is stored

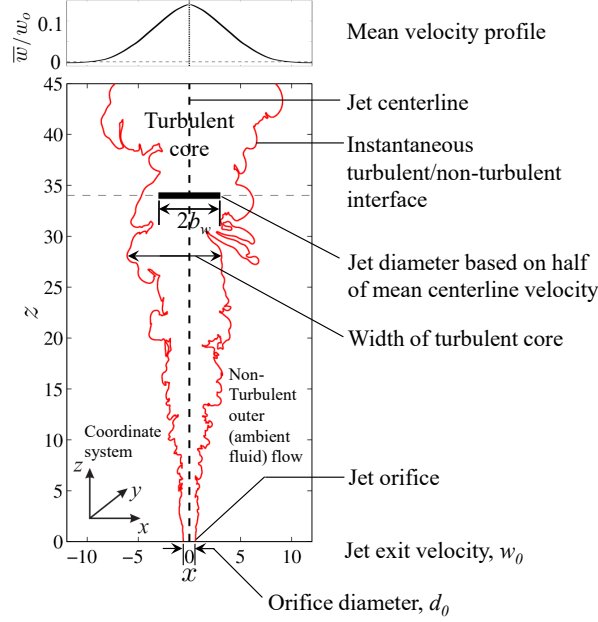


FIG. 1. Diagram of an axial section to illustrate main terminology and notation for jet flow. (See additional explanation in text.)

in the cell center and the velocity components are stored on the cell faces [24]. More details on the scheme and the code are discussed in Prasanth (2014) [26]. The computational domain extends up to $z = 55$ in the streamwise (z) direction and -50 to $+50$ in the cross-stream directions (x, y). The total grid size is $480 \times 480 \times 600$ in the x, y and z directions respectively (yielding 138 million grid points in all). In the streamwise direction the grid size varies from 0.05 at the orifice to 0.18 at the outflow. In the cross-stream plane the grid is uniform (of size 0.05) from $x, y = -9.25$ to $+9.25$, thus ensuring adequate resolution in the turbulent core; beyond this the grid is gradually stretched towards the lateral side walls. The mean viscous dissipation $\bar{\epsilon}$ is calculated from the fluctuating strain rate s'_{ij} as

$$\bar{\epsilon} = 2\nu \overline{s'_{ij} s'_{ij}}, \quad (3)$$

$$s'_{ij} = \frac{\partial u'_i}{\partial x_j} + \frac{\partial u'_j}{\partial x_i}, \quad (4)$$

where the primes denote fluctuating quantities ($u'_i = u_i - \bar{u}_i$, etc.) The velocity derivatives are calculated using a second order central differencing scheme. The Kolmogorov and Taylor microscales are respectively given by

$$\eta = \nu^{3/4} \bar{\epsilon}^{-1/4}, \quad (5)$$

$$\lambda = (15\nu \overline{w'^2} / \bar{\epsilon})^{1/2}, \quad (6)$$

where $\overline{w'^2}$ is the turbulence intensity in the streamwise direction. The dissipation (normalized using $w_c^3/(z - z_0)$, where z_0 is a virtual origin) near the jet centerline at $z \approx 33$ in the present simulation is 0.18, to be compared with 0.18 reported by Panchapakeshan & Lumley [27] at $Re = 11,000$, 0.22 by Bogey & Bailly (2009) [28] at $Re = 11,000$ and 0.25 by Taub *et al.* (2013) at $Re = 2000$ [29]. At $z/d \approx 33$ near the jet center-line, $\lambda/b_w \approx 0.2$, to be compared with 0.18 ([10], round jet, $Re = 2000$, center-line). The Kolmogorov length scale (η) at $z \approx 33$ is about $0.04 d_0$, and the corresponding grid size in the x, y, z directions is approximately η, η and 3η respectively.

The bottom plane at $z = 0$ outside the orifice is treated as a no-slip wall in the plane of the orifice exit. A fixed, uniformly distributed disturbance of 5% amplitude with zero mean is superposed on the top hat velocity profile at the orifice to trip the flow to a turbulent state. The disturbance is superposed only on the streamwise velocity component,

however, and at a random set of points also chosen from a uniform distribution over the orifice area. At the outflow boundary we use the zero normal derivative condition for all the variables, with a layer of viscous padding from $z = 52$ to $z = 55$ to ensure smooth exit of the turbulent flow from the computational domain. The lateral boundaries of the computational domain are also treated as no slip walls, but (at $x, y = \pm 50$) they are sufficiently far away from the jet axis to have any significant effect on the momentum balance. The net momentum flux $\int (\overline{w^2} + \overline{w'^2} - 0.5[\overline{u'^2} + \overline{v'^2}])dS$, where the overbar denotes time average, prime denotes fluctuation and the domain of integration is $-50 \leq x, y \leq 50$, is conserved to better than 99% over the whole domain in the z direction (Shinde *et al.* (2019) [30]). Other details about the solver and its validation are discussed in Prasanth (2014) [26]. The simulation took up to $t = 900$ to attain a stationary state. Data for computing flow statistics was acquired over the time interval $900 < t < 2650$. The simulation was run on 108 nodes of the 360 TF supercomputer at CSIR-4PI, Bangalore.

III. DATA ANALYSIS

The mean streamwise component of the velocity at r, z is computed as

$$\lim_{t \rightarrow \infty} \frac{1}{t} \int_{t_1}^{t_2} \frac{1}{2\pi} \int_0^{2\pi} \mathbf{w}(r, z, \phi, t') d\phi dt' = \overline{\mathbf{w}}(r, z), \quad (7)$$

where $t_1 = 900$, $t_2 = 2600$, $t = t_2 - t_1$, and ϕ is the azimuthal angle. It is found that the jet is in a self-similar state over the range $27 \leq z \leq 40$ to within 0.6% in the mean velocity ($\overline{w}/\overline{w}_c$) and in an equilibrium or self-preserving state over the range $32 \leq z \leq 36$, the maximum in $(\overline{w'^2}/\overline{w_c^2})^{0.5}$ and Reynolds shear stress $-\overline{w'u'}/\overline{w_c^2}$ vary less than 1% and 1.5% respectively. Additional details on the statistics are available in Shinde *et al.* (2019) [30].

We present here analyses of the solutions for the vorticity field within the turbulent jet and the velocity field outside a suitably determined ‘edge’ of the turbulent core of the jet, defined as the contour surface of a specified threshold value of the vorticity modulus,

$$|\boldsymbol{\omega}(\mathbf{x}, t)| = \sqrt{\omega_x^2 + \omega_y^2 + \omega_z^2} \quad (8)$$

in terms of its Cartesian components. Vorticity-based criteria are particularly appropriate as the essential characteristic of any turbulent flow is a time-dependent stochastically varying vorticity field, which is logically a more fundamental parameter than the scalar concentration field of a flow-visualizing dye, often used in experiments (e.g. [15], [10], [5]). The definition of the edge is determined as a characteristic value of $|\boldsymbol{\omega}|$ connected with the interface layer of relatively rapid change that is encountered as a test point moves inward toward the jet core from the ambient (nearly) irrotational flow (see Fig. 1). Based on extensive studies of these vorticity profiles across the edge (Shinde *et al.* (2018)), it is found convenient to introduce two distinct edges or boundaries of the jet. The first is located at the ‘middle’ of the T/NT interface at $|\boldsymbol{\omega}| = 0.5$, beyond which $|\boldsymbol{\omega}|$ varies rapidly to 1.0 or above in the turbulent core. This defines the ‘inner’ boundary of the turbulent jet.

For reasons that will be clear shortly, we find it necessary to define an ‘outer’ boundary at $|\boldsymbol{\omega}| = 0.1$, which similarly locates the rotational / irrotational (R/IR) boundary of the jet. The basis for this choice will not be presented here in detail, chiefly because the images shown in the rest of the paper provide ample supporting evidence for the choices made (see Sec. IV). The contour surfaces $|\boldsymbol{\omega}| = 0.1$ and 0.5 will thus be referred to in the sequel as the outer and inner boundaries of the jet respectively. There have been other proposals for defining two boundaries, using slightly different criteria. Reeuwijk & Holzner (2014) [14] define an inner and outer boundary that separate the turbulent core from the buffer region and the VSL from the buffer region respectively. The inner boundary in their analysis represents the enstrophy threshold for which the interface propagation velocity v_n is zero and the outer boundary represents the threshold below which the enstrophy production is negligible.

In most of the images of jet cross-sections presented here, it has been found illuminating to include a background vorticity field within the core of the jet. Depending on the purpose of the analysis being carried out, different choices may be made for the particular measure of vorticity that is most appropriate for the analysis. Thus ω_z may be more relevant in a diametral section. Similarly, in an axial section in the $x - z$ plane at $y = 0$, either the modulus $|\omega_y|$ or the signed value of ω_y or the azimuthal component ω_ϕ may be more appropriate.

The axial section is taken over the range $23 \leq z \leq 45$. The flow is also studied in two diametral planes, one at $z = 34.05$ which lies exactly in the middle of the self-preserving zone, and the other at $z = 42.69$.

IV. JET BOUNDARIES

We shall now present the results derived largely from an analysis of axial and diametral sections. Particular attention is given to possible connections between the flow-field outside the jet boundary and the vorticity field within the jet. Only a limited number of 2D sectional data are analyzed, as this is adequate for the conclusions drawn here. A more detailed analysis, including that of selected 3D velocity and vorticity fields will be reported separately.

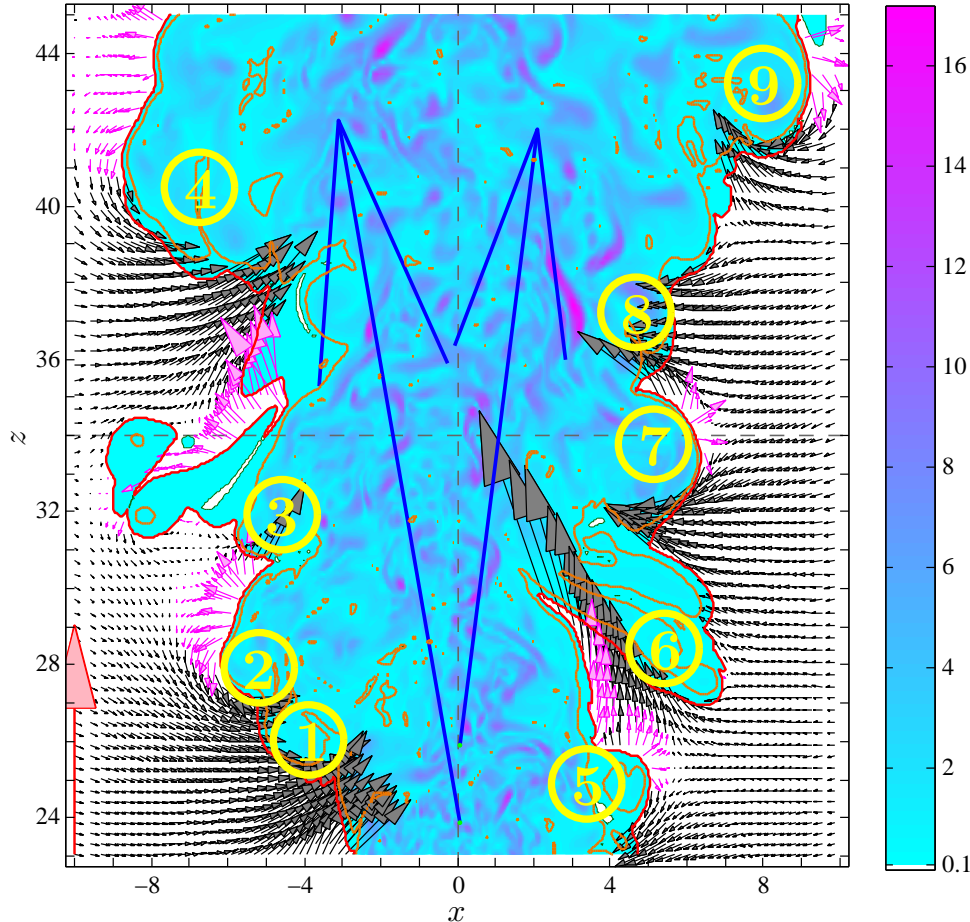


FIG. 2. Axial section in the xz plane at $t = 925$, showing the instantaneous velocity and total vorticity modulus $|\omega(\mathbf{x}, t)|$ fields. The black and pink velocity vectors (respectively with radially inward and outward components) are shown only in the ambient beyond the outer boundary of the jet, represented by the red contour at $|\omega| = 0.1$; the orange contour at a threshold of 0.5 represents the inner boundary). For comparison two typical flow velocity vectors (blue) inside the core of the jet near the jet centerline are plotted. To avoid clutter, only every fourth velocity vector in the x -direction and every third in the z -direction are plotted. The red vertical arrow at the bottom-left corner is a reference velocity vector of magnitude $0.1w_0$.

The axial sections of the jet flow used in the analysis below are within the self-similar region of the jet ($27 \lesssim z \lesssim 40$). We begin with Figure 2, which shows an axial cross section of the jet with contours of $|\omega|$ in the turbulent core. The yellow circles circumscribing the numbers indicate the sub-regions (henceforth referred to as ‘SR’ followed by the number) where significant entrainment activity appears to be taking place. Following the inner boundary, we can discern in Fig. 2 a complete coherent structure with a base along a 2-6 line (i.e., joining SR2 and SR6), narrowing to a small nose around $z \approx 38$ penetrating the larger downstream structure (of which we see only the bottom third) at its base along the line 4-9. These have a strong resemblance to structures observed in experiments (e.g., Mungal & Hollingsworth [31]) and other numerical simulations (e.g., Basu & Narasimha [32]). There is a similar penetration by the upper third of the upstream structure along the base 2-6 of the central structure. The core of the central structure ($30 \lesssim z \lesssim 38$) slopes slightly rightwards whereas the upper structure has a tilted base 4-9 sloping up towards the left. On the whole, the core of the jet appears to be in a helical mode (of the kind observed by Dimotakis *et al.* (1983) [5], Mungal and Hollingsworth (1989) [31]). It is known from studies like the wavelet analysis of Narasimha *et al.* (2002)

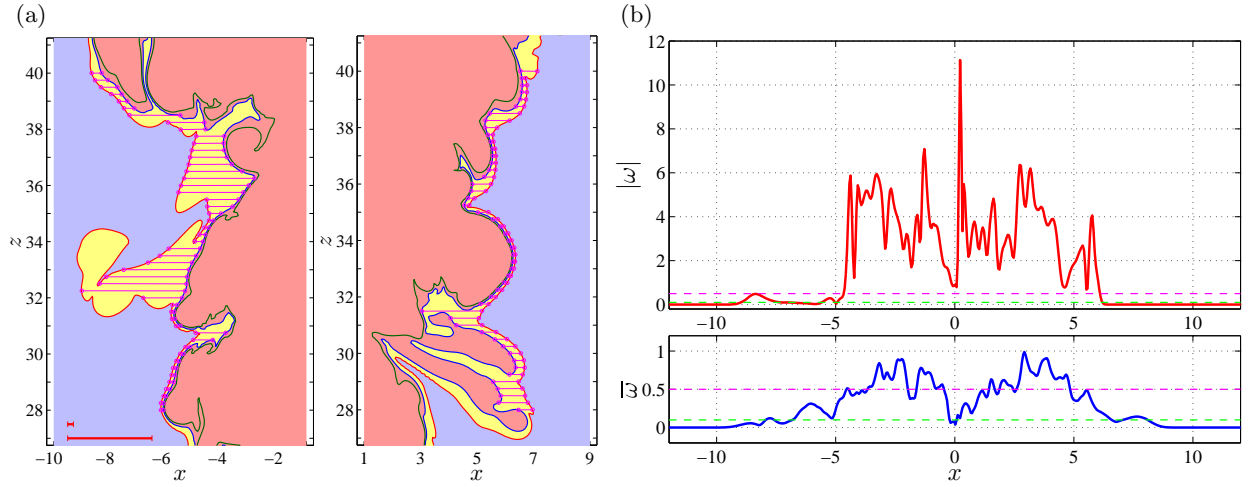


FIG. 3. (a) Axial section in the xz plane at $t = 925$. The $|\omega| = 0.1$ and 0.5 contours in the axial cross section of Fig. 2 showing the wide variability in the separation distance between the two contours that bound the yellow region; the lighter reddish region is the turbulent core, the lighter lavender region is the ambient. The red, blue and dark green boundaries are marked respectively at thresholds $|\omega| = 0.1, 0.5, 1$. The thick red horizontal lines at the bottom in the left panel show 5η (short line) and 5λ (long line). (b) A typical variation of the normalized instantaneous vorticity modulus $|\omega|$ (in red), compared with the time-averaged vorticity modulus, $|\bar{\omega}|$ (in blue). The bumps in $-10 < x < -5$ correspond to the two intersections of the line $z = 34.05$ with the outer viscous buffer zone. The broken horizontal lines are marked at 0.1 (green) and 0.5 (pink).

[33] that the base of the structure is likely to be a fluted vortex ring with ambient fluid below the base being drawn into the structure through the Biot-Savart relation.

Figures 3 (a) and (b) respectively present axial sections near the edges of the jet and the distribution of $|\omega|$ across a diameter of the jet. From Fig. 3 it is seen that there is a relatively rapid change in $|\omega|$ values as the T/NT interface at the inner boundary $|\omega| = 0.5$ is crossed by a test point moving towards the turbulent core. However, it is also seen that the separation between the contours of $|\omega| = 0.5$ and $|\omega| = 0.1$ can vary appreciably at certain locations along the boundary of the jet. For example, in Fig. 3(a) the inner and outer boundaries are close to each other in some areas (e.g., $-8 < x < -6$, $38 < z < 45$) and well separated in others (e.g., $-8 < x < -3$, $31 < z < 38$). In the latter case we shall call the region between the inner and outer boundaries an ‘outer buffer zone’, to be distinguished from the buffer zone defined by Reeuwijk and Holzner [14] in a plane jet, which possibly is inwards of the present inner boundary, and will here be called the ‘inner buffer zone’. The threshold values used for defining the boundaries by Reeuwijk & Holzner (2014) [14] are not applicable here as these thresholds are a function of Reynolds number and also of the dimensionality and nature of the flow. Figure 3(a) shows how the distance between the two boundaries varies along the inner boundary of the jet. A measure of this distance is the separation along the x axis from the inner to the outer boundary on either side of the jet. It is seen that this inter-boundary separation varies from 0.090 to 3.67 in the left boundary and from 0.077 to 2.13 in the right boundary.

For comparison, estimates of the two relevant scales in the problem, namely the Kolmogorov length and the Taylor microscale, are shown in Fig. 3(a) at $z \approx 33$, $x, y = 0$. It is seen that inter-boundary separation varies from the order of the Kolmogorov scale to the Taylor microscale; however, the changes in $|\omega|$ from 0.5 toward 1.0 and above in the turbulent core is almost always sharp, and has a length scale comparable to the Kolmogorov scale. Figure 3(b) makes this point by displaying the variation of the total vorticity modulus $|\omega|$ at $z = 34.05$. For comparison the magnitude of the mean flow vorticity is also shown in the figure. It is first of all seen that the fluctuating vorticity $|\omega|$ in the core can be an order of magnitude larger than the mean. Furthermore, while the T/NT interface at $x = 6.5$ drops steeply from about 4.0 to nearly 0 , the interface near $x = -5$ drops steeply all the way to about 0.5 , then becomes less steep, and finally takes the form of two noticeable but smooth bumps, the one farther away being the bigger. From comparison with Fig. 2 and Fig. 3 (a) the bumps correlate with the outer buffer zone with its small but apparently non-turbulent vorticity (as we shall shortly demonstrate). In the light of the many discussions on this issue in the literature [10, 11, 34–36] we conclude that both scales seem to have a role to play, from the sharp T/NT interface layer of thickness $\mathcal{O}(\eta)$ to the larger lateral extent of the viscous buffer zone with a dimension of order λ . Understanding the role of these different scales and whether this difference in scales persists at higher Reynolds requires further investigation.

Nature of the vorticity field from the T/NT to the R/IR interface

Beyond the outer boundary at $|\omega| = 0.1$, the flow is nearly irrotational. It is seen (Fig. 2) that the core of the jet

has $|\omega|$ values ranging from 1.0 to more than 17 over much of the cross-section, except in the very short section of length $\Delta x \simeq 2$ at $z \simeq 25$ to 28. This could mark the region of separation between two successive coherent structures in the jet, as may be inferred from jet flow visualizations by the PLIF technique [5], or by examining the computed vorticity field of Basu & Narasimha [32] in a temporal round jet. Another such separation between two successive structures is seen in Fig. 2 around $z \simeq 38$ to 40. Here, the base of the structure is on the 4-9 axis, and clearly carries a vortex ring, as we can infer from the velocity field in the ambient. Taken together, this lends further support to the view that the flow exhibits a helical mode.

As expected, the edges of the jet are highly convoluted (especially the inner boundary, which is a fractal curve (Sreenivasan & Meneveau (1986) [37] and Sreenivasan *et al.* 1989 [38])). Figure 2 includes the velocity field in the xz plane outside the inner edge of the jet. The arrows in dark gray indicate a radially inward component, and those in pink a radially outward component. A few long arrows within the core (with large heads) are also shown, to give an idea of the relative values of the velocity magnitudes within and outside the boundary of the jet. It is seen that in most of the selected sub-regions the velocity vectors crowd into a part of the jet boundary (dark gray arrows), and represent entraining motions. In some cases (above SR1, near SR4, between SR5 and 6) there are some pink arrows as well, which could be detraining motions, but these are generally locally diverging radially outward motions compared to the radially inward converging and entraining motions. Whether the motions entrain or detrain also depends upon the propagation velocity of the interface. However, Wolf *et al.* [12] and Reeuwijk & Holzner [14] have shown that the interface velocity is of the order of the Kolmogorov velocity, so generally negligible (at $z \approx 33$, Kolmogorov velocity is $\approx 0.01\bar{w}_0$). It will be seen that there is little evidence for a parallel inward flow in the ambient impinging on the jet boundary; instead, entrainment often seems to occur in relatively intense events concentrated in a few narrower areas near the edge (for example, below SR1, SR4, SR7 and SR9; this is further discussed in section V). In these areas the flow velocities can go up to 0.4 times the mean centre-line velocity \bar{w}_c (e.g., in SR7). Thus the fluid is pushing the turbulent edge inward and rushing into the turbulent core across the T/NT interface through ‘gulfs’ or ‘wells’ created by the inrush of ambient fluid. (This is best seen in movies of the flow; see the short sequence of stills in Fig. 4.) In all these cases the streamlines in the outer flow exhibit, in part, one or two roughly circular patterns near the entraining areas, suggesting that they represent a velocity field induced by relatively strong vorticity in the near core (see analysis of SR9 in sec. V). Occasionally, however (see e.g. the region between SR2 and SR3), the flow appears to be radially organized, indicating a source-like flow, which we shall further discuss below.

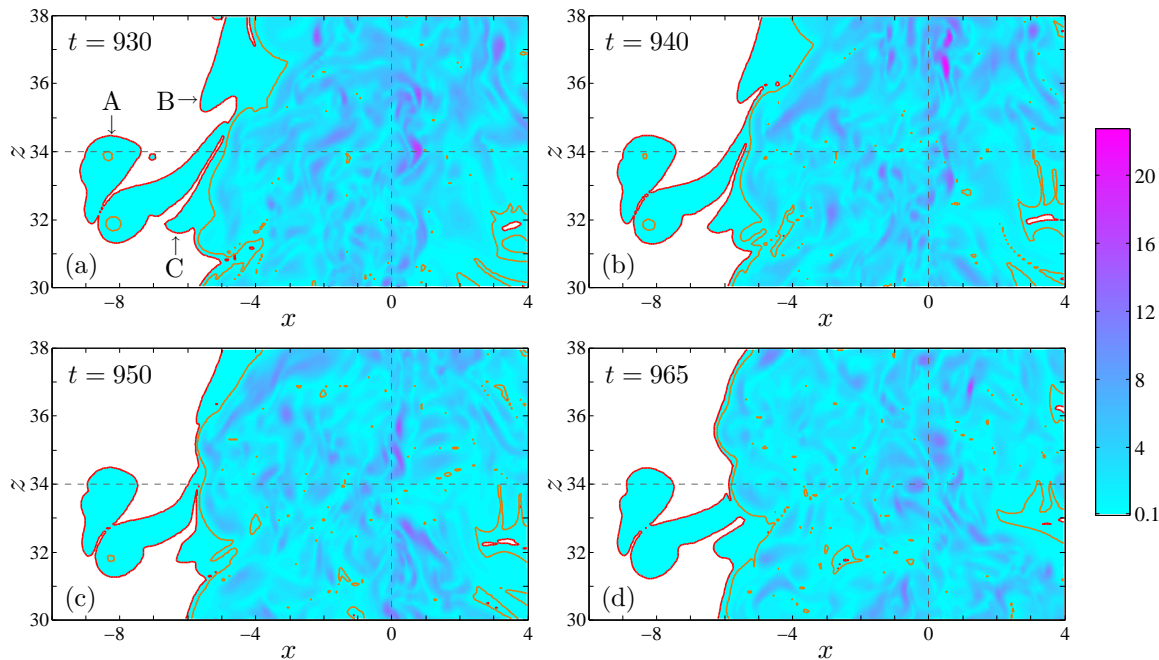


FIG. 4. Temporal evolution of a part of the jet from Fig. 2. Three areas in the figure labeled as A, B and C illustrate important features of the evolution (see text for discussion).

Figure 4 shows the time evolution of a part of the jet ($32 < z < 36$) that is accurately self-preserving. Region A hardly changes in shape or in vorticity range over the whole time interval $930 \leq t \leq 965$ covered by the images. On the other hand, region B keeps continuously shrinking, and has disappeared at $t = 965$. This disappearance is largely due to the outward motion of the inner boundary till, in (d), the two boundaries are very close to each other in the

interface above $z = 34$. Region C undergoes minor changes in shape, in part again because of the outward movement of the inner boundary. Between (a) and (d) it is seen that the turbulent core has expanded, with a general reduction in the larger vorticity-sparse areas seen near the boundaries in the earlier images.

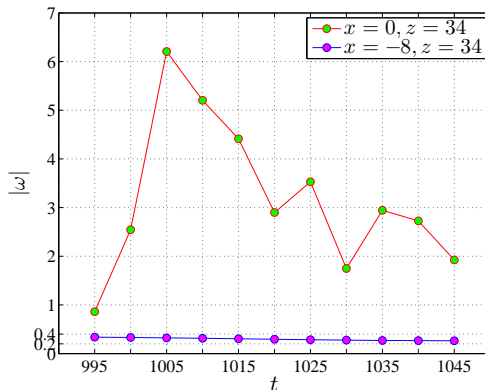


FIG. 5. Temporal variation of the total vorticity modulus at two points in the plane $z = 34$, one on the centerline $(0, 0, 34)$ and the other at $(-8, 0, 34)$ in the outer buffer region between the inner and outer boundaries.

Figure 5 compares the variation of $|\omega|$ with time at two points. The vorticity at the center line shows substantial variation in time, whereas that in area A in the outer buffer zone is more than an order of magnitude lower and exhibits a slow and gentle decay with hardly any fluctuation that can be associated with turbulence. This justifies why such a buffer zone can be characterized as ‘viscous’, and the structure at zone A in Fig. 4 may be called a ‘viscous tongue’, most probably a relic or fossil from an earlier excursion of in- or out-of-plane vorticity from the core or buffer zone into an ambient nearly at rest.

V. STRUCTURE OF THE AXIAL SECTIONS AT SELECTED SUBREGIONS

To analyze the relation between the vorticity field in the turbulent core and the velocity field beyond the R/IR boundary, we consider selected subregions in axial and diametral planes. We start with the axial sections, namely SR 9, 1, 4 and 7.

SR9: This offers the simplest flow situation among those seen in Fig. 2 for the following reasons illustrated in Fig. 6. (Note that the back-ground vorticity field displayed in Figs. 6 - 8 is the signed azimuthal component ω_ϕ , which is helpful in correlating the velocity field in the ambient with the vorticity field in the core.) The dominant feature of the flow within the jet core in SR9 in Fig. 2 is a large lump of clockwise (negative, blue) vorticity. A diametral section of the jet around SR 9 at $z = 42.69$ is shown in Fig. 6(a). By comparing with Fig. 2, it is seen that this diametral section of the core flow in SR 9 contains an ovoid around $x \approx 8$, $-1 < y \leq 1.5$, with x, y, z dimensions of about $2 \times 5 \times 2$. Thus the variation of the vorticity with y in the central region of the ovoid is not very strong. From Fig. 6(b), which is a zoom on SR 9 in Fig. 2, it is seen that the highest azimuthal vorticity ($|\omega_\phi| = 6.8$) is confined to a nearly circular region of diameter less than 1.0. The maximum in the other components of vorticity are about a fifth of that of ω_ϕ . Although the structure is 3D, the azimuthal component dominates over the other components of vorticity, so to a first order approximation we can treat it like a 2D flow. The image clearly indicates that there is a circulating motion around the vortex in a direction that is consistent with the sign of the vortex. Very close to the region where vorticity is intense and of one sign over the region (as often happens in coherent structures) there appears to be relatively high correlation between the vorticity and velocity fields. Figure 6(b) thus depicts a strong circulatory motion, first hugging the outer boundary and then penetrating the inner boundary.

Figure 6(c) shows instantaneous effectively 2D streamlines in the xz plane for SR9 starting from points located along $z = 42.5$, corresponding to the flow field in Fig. 6(b). Note that all these streamlines start from neighboring grid points (closer to each other in the core than in the ambient, see Sec. II), and therefore do not represent equal differences in the stream function. The red and black contours are the same as in Fig. 6(b). A ‘dividing’ streamline, separating fluid which spirals back into the vortex from fluid that moves away, is shown in pink. Such an interpretation is encouraged by the weak variation of vorticity in the y -direction, making the flow close to a 2D field as already noted.

From Fig. 6(c), with vorticity in the object peaking at $x = 8.28$, $y = 0$, $z = 42.69$, the domination of the azimuthal vorticity in determining the velocity field in the neighborhood is understandable. This is further supported by Fig. 6(d),

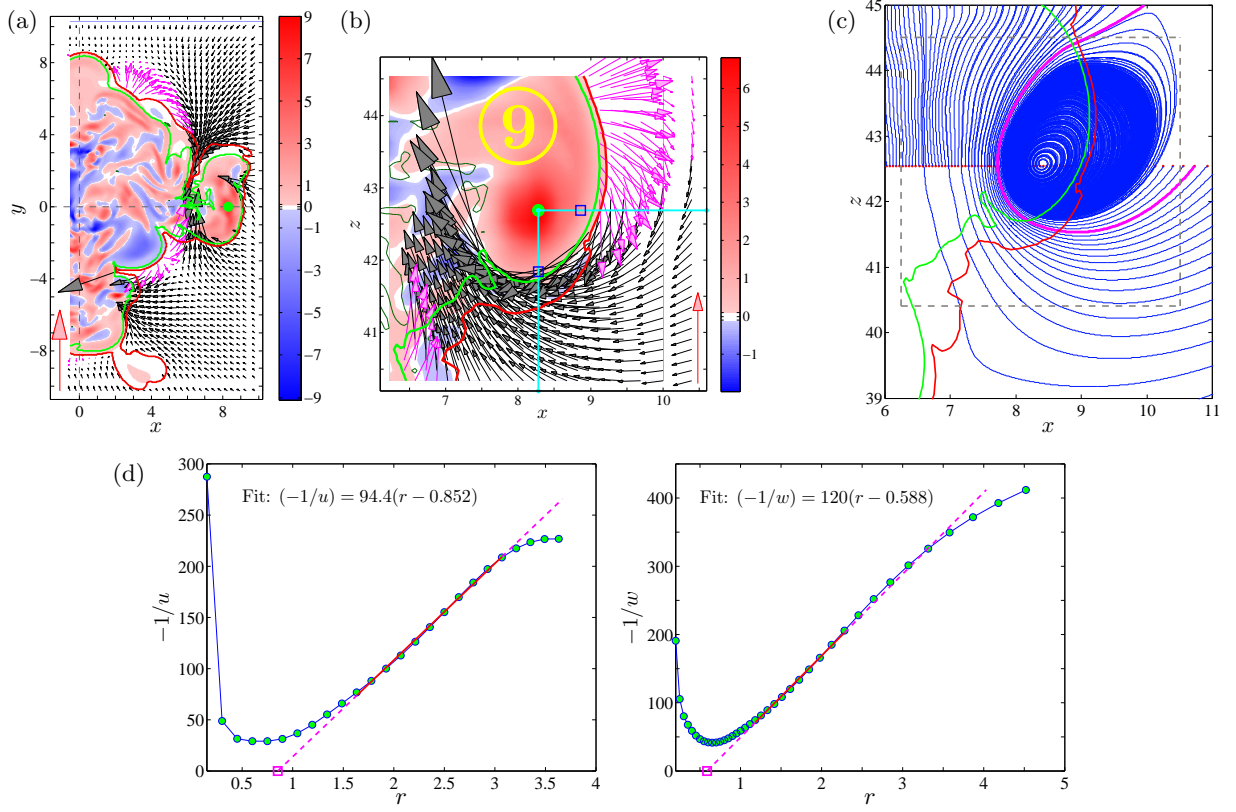


FIG. 6. (a & b) Instantaneous velocity in the ambient fluid and azimuthal vorticity (ω_ϕ) field at $t = 925$. Red and blue colors indicate clockwise and counterclockwise vorticity respectively. The red and green lines show the outer and inner jet boundaries respectively at thresholds 0.1 and 0.5 based on $|\omega|$. The green dot is nominal center of the red vorticity patch (see main text). Two ticks on either side of zero on the color-bar correspond to $+0.1$ and -0.1 . Black vectors show inward velocity, while the pink vectors indicate outward flow velocities. The reference velocity vector shown in red color at the bottom-left corner of (a) is $0.05w_0$ and at the bottom-right corner of (b) is $0.025w_0$. To avoid clutter, only every seventh velocity vector is plotted in (a) and every third in the x -direction in (b). (a) A portion of the diametral section at $z = 42.69$ showing a vortical object at the right around $x = 8$. (b) Zoomed-in view for SR9. (c) Instantaneous streamlines for SR9 starting from $z = 42.5$. The pink curve marks the streamline separating the fluid spiraling into the vortex from that which drifts away from the vortex. The dashed grey rectangle marks the zoomed portion shown in (b). (d) The inverse velocity relation with distance along the horizontal (left panel) and vertical (right panel) lines drawn in (b) showing a region of $1/r$ decay like that due to a line vortex normal to the xz plane at the location of the green dot (nominal centre).

which shows a plot of the reciprocal of the magnitude of the w and u components of the velocity respectively in the xz and yz planes, as a function of radial distance r from an approximate origin along the lines $z = 42.69$ and $x = 8.28$ respectively (shown by cyan colored lines in Fig. 6b). A linear fit is a good match to the data over the range of r between 1.6 and 3.2, as marked by dashed red lines; the equations for the fits are shown on the respective plots. This supports the conclusion that the outer velocity field approximates to that induced by a line vortex along the y -axis, by the Biot-Savart law. By extending the fitted line to the zero of the inverse of the velocity, we can identify an “effective center” for the vortex (marked by pink squares in Fig. 6d). The fact that these effective centers are not identical but not very far from each other (separation about 0.3) is consistent with the finite size and the imperfect symmetry of the vortical structure seen in Fig. 6(a).

SR1 & 2: Figure 7(b) (the azimuthal vorticity field alone is shown in Fig. 7(a)) illustrates how the ambient velocity field maybe understood in terms of two anticlockwise vortices next to each other near the inner boundary. In SR2 the vorticity is anticlockwise near the edge but clockwise away from it further inward. The net effect of this somewhat more complex vorticity field is that in the region $28 < z < 29$, $-7 < x < -6$, the flow in the ambient is away from the jet (pink arrows), with only a mild contribution to the inward circulatory motion. In the zone $26.5 < z < 27.5$, however, the motion is more strongly circular in the lower parts of SR2.

SR4: Here (Fig. 7(c)) the vortices in the upper reaches $38 < z < 42$ resemble the region near SR2 in Fig. 7(a). Because of the weaker clockwise component in the vertical strip $38.2 < z < 41.8$, $-7.5 < x < -6.5$, the flow in

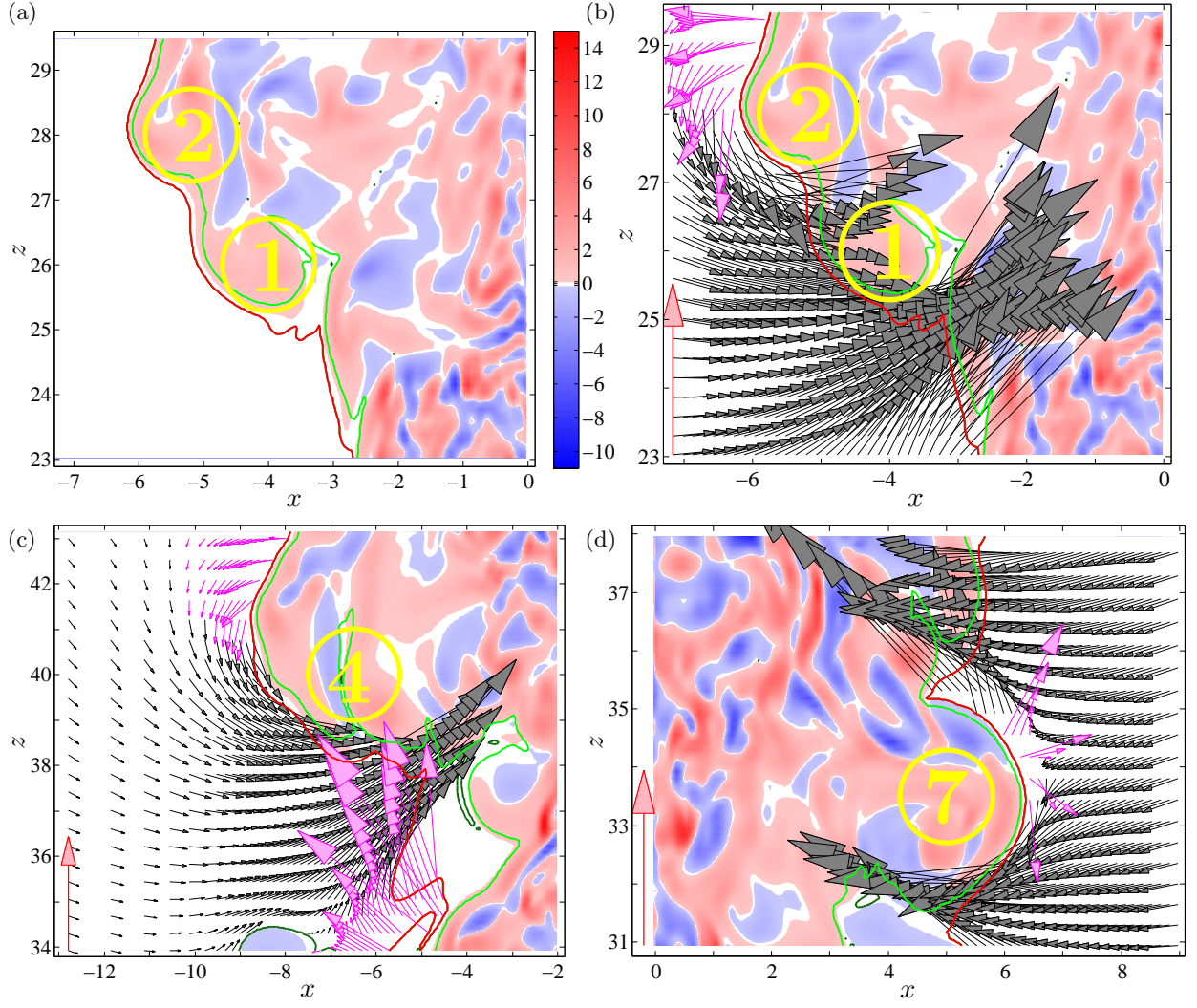


FIG. 7. Ambient velocity and core azimuthal vorticity (ω_ϕ) fields, showing the inrush of flow into the core of the jet from the ambient fluid. All other conventions are the same as in Fig. 6(b). (a) SR1, SR2 (ω_ϕ) field (b) SR1, SR2, with inrush velocity field in the ambient with the (ω_ϕ) field; the tick marks shown above and below zero on the color-bar indicate respectively $\omega_\phi = +0.1$ and -0.1 (c) SR4, (d) SR7. Magnitude of the reference vector shown in red at the bottom-left corner of (a, c, d) is $0.025\omega_0$. Color-bar shown in (b) also applies to the vorticity contours shown in (a, b, c, d).

$37 < z < 40$ is dominated by counterclockwise vorticity.

SR7: Fig. 7(d) is the most complex image among the ones selected here for analysis. There is first of all the clockwise motion at the lower levels of SR7 ($31.5 < z < 32.2$, $3.5 < x < 6.5$). Similarly there is a counter-clockwise circulation in the upper levels of SR7 ($34.3 < z < 36$, $3.5 < x < 6.6$). It is clear that the former is strongly influenced by the large region of clockwise vorticity in the lower half of SR7, and the latter is attributable to the clockwise circulation due to the vorticity of the same sign in the block $34 < z < 36$, $4.5 < x < 6$. The large values (up to $0.4\bar{\omega}_c$) of the inrush velocities here may compensate for the small area at the entrance to the gulf ($\sim d_o$), and hence can make a non-negligible contribution to the entrainment rate.

The above four examples show some of the different types of organized motion that occur due to interactions between vortex elements that are part of the coherent structures in the core fluid, and the Biot-Savart induced velocity due to these elements at the T/NT interface. The most striking feature of the flow in the ambient is that it is organized largely in terms of interacting circulatory motions. Roughly speaking the diameter of the region containing this ordered outer motion is about $20 d_0$ at $z \simeq 40$ to 44 , and about $12d_0$ at $z \sim 28$. This is approximately twice the local diameter of the turbulent core. These estimates of the spatial extent of the velocity and vorticity structures involved in the interaction are a strong indication that they are related to *elements* of the large-scale vorticity in coherent structures in the core flow, and cannot be attributed to small scale vorticity.

Zone	Flow events based on images in Fig. 8(a-d) and an image at $t = 975$ not included in Fig. 8
A	<ul style="list-style-type: none"> • Mild inrush at $t_0 = 925$, gets deeper but bigger, begins to connect with H by $t = 950$
B	<ul style="list-style-type: none"> • Starts with outflow at t_0. • Boundary pushed outward by vorticity in the turbulent core, gradually disappears by $t = 975$
C	<ul style="list-style-type: none"> • Starts at t_0 with mild inrush, grows slowly and covers CD region in a broad inrush by $t = 970 - 975$
D	<ul style="list-style-type: none"> • Radial outflow prominent at t_0, decays slowly, disappears at $t \simeq 970/975$. • Boundary is advancing throughout.
E	<ul style="list-style-type: none"> • Modest outflow capped by inrush at bottom of D and lower part of E at t_0. • Upper part from D weakens, outflow disappears by $t = 950$. • Lower E squeezed by expansion of core. • Weak outflow reappears at E at $t = 975$.
F	<ul style="list-style-type: none"> • Mild inrush at t_0, little change even at $t = 975$.
G	<ul style="list-style-type: none"> • Modest outflow at $t = 925$, pushed out by both inner and outer boundaries (which remain close to each other). • Spans almost whole quadrant [from $(-2, -6)$ to $(7, 0)$] by $t = 955$. • Shrinks by $t = 965$, making room for new inrush at H, but still active at $t = 975$.
H	<ul style="list-style-type: none"> • Inrush moves right, gets weaker by $t = 955$. • A and H inrushes appear to coalesce (from opposite directions), and become a major feature of the flow by $t = 970/975$, like C.

TABLE I. Flow events across a diametral plane

This analysis may be compared with two others in the literature. Phillip and Marusic (2012) [16] show, in a ‘caricature’ of a turbulent jet and the entrainment (their Fig. 6), a flow of the ambient fluid towards the turbulent core in parallel streamlines almost till they impinge on the edge of the jet, in contrast to the ordered motion we see here in Figure 2. Westerweel *et al.* (2009) [10] showed an instantaneous velocity field (Fig. 19 in their paper) that appears (in one part of the domain covered in the diagram) to transport turbulent fluid out of the turbulent core across the interface into the ambient. However, in a frame of reference fixed with respect to the vortex within the core, the velocity vectors were almost parallel to the interface. Thus, they concluded that organized motions do not transfer irrotational fluid into the turbulent core. In the immediate neighborhood of the vortex, however, the relative velocity induced in the ambient fluid appears to be crossing into the core. It is thus seen that the picture presented by the present DNS analysis is quite different from conclusions drawn by experimental results which may be affected by the limitations of PIV measurements in the low-velocity irrotational region.

VI. ANALYSIS OF DIAMETRAL SECTIONS

Figure 8 presents a sequence of images of the diametral section at $z = 42.69$ at four different instants ($t = 925, 950, 960$ and 970). As before the ambient velocity field is presented against a background of the vorticity field ω_ϕ within the turbulent core.

The inner and outer boundaries of the jet are indicated as before by contours of $|\omega|$ at 0.5 and 0.1 respectively. As with axial sections, we see in Fig. 8 regions where the inner and outer boundaries are very close to each other, as well as other regions where they are much farther apart. The flow field in the ambient is of two distinct types, the dominant one being radially outward motions, with circulatory motion also present but not as strong as in the axial section of Fig. 2. The radial motions often issue from those regions where the inner and outer boundaries are close, for the simple reason that core-flow vorticity elements are then close to the ambient fluid. For the same reason circulatory motions may also be present in such an area (see for example Fig. 6, and also the area straddling the x axis at $y = 0$ across the first and fourth quadrant in Fig. 8).

The diametral section shown in Fig. 8(a) is just above the wide base S4-S9 of an existing coherent structure, the lower part of which is seen near the top around $z \simeq 38$ to 42 in Figure 2. The strong source-like radially outward motion seen in the ambient fluid across the second and third quadrants, $-9 < x < -5$ which we call zone A, has a striking degree of circular symmetry, and which is not entirely consistent with the azimuthal component of vorticity shown in Figure 8(a). A plausible explanation involves the effect of streamwise vorticity which has not been considered so far. Figure 9(a) shows data at the same stations as in Fig. 8(a), except that at each of the four stations, the azimuthal component of vorticity is replaced by the streamwise component. Figure 9(a) shows the presence of a pair of streamwise vortices in zone A (red:counter-clockwise and blue:clockwise). The arrangement of these streamwise

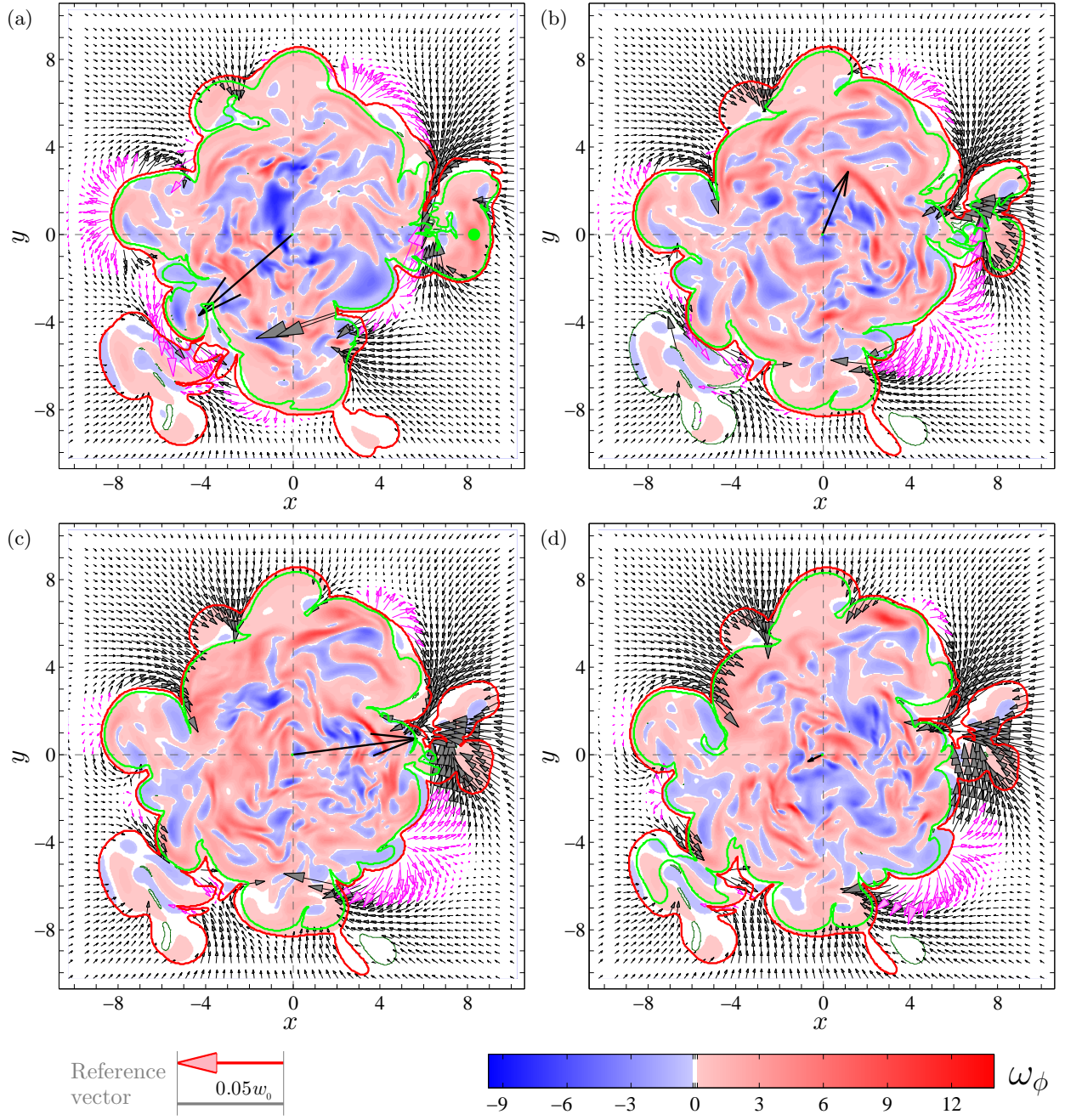


FIG. 8. Four instantaneous diametral sections of images at $z = 42.69$ at times $t =$ (a) 925, (b) 950, (c) 960, (d) 970. The vorticity field in these images is the signed azimuthal component ω_ϕ . Thick black vector indicates velocity inside the jet at $(0,0)$. The two ticks, one on each side of zero on the color-bar, correspond to $+0.1$ and -0.1 . To avoid clutter only every seventh velocity vector is plotted.

vortices along with the local azimuthal vorticity result in an outward movement of the fluid between the vortices from the turbulent core towards the T/NT interface, which in turn results in an instantaneous displacement effect (note that the inner and outer boundaries are very close to each other and are pushed outward along with the fluid). This boundary expansion is also evident from a comparison between Fig. 8(a) and Fig. 8(b). Interestingly, a somewhat similar radial flow is noticeable in the fourth quadrant of Figs. 8(a-d). Also, the vortical object of SR9 (Fig. 6) is clearly seen in the diametral section in Fig. 8(a) where its length along the y axis is seen to be about 5. However, the feature gradually changes its shape with time, and is substantially different at $t = 970$ (Fig. 8(d)). Between the data in Figs. 8(a) and Fig. 6(a), it can be confirmed that the vorticity in the object around the point $x \approx 0$, $y \approx -7$

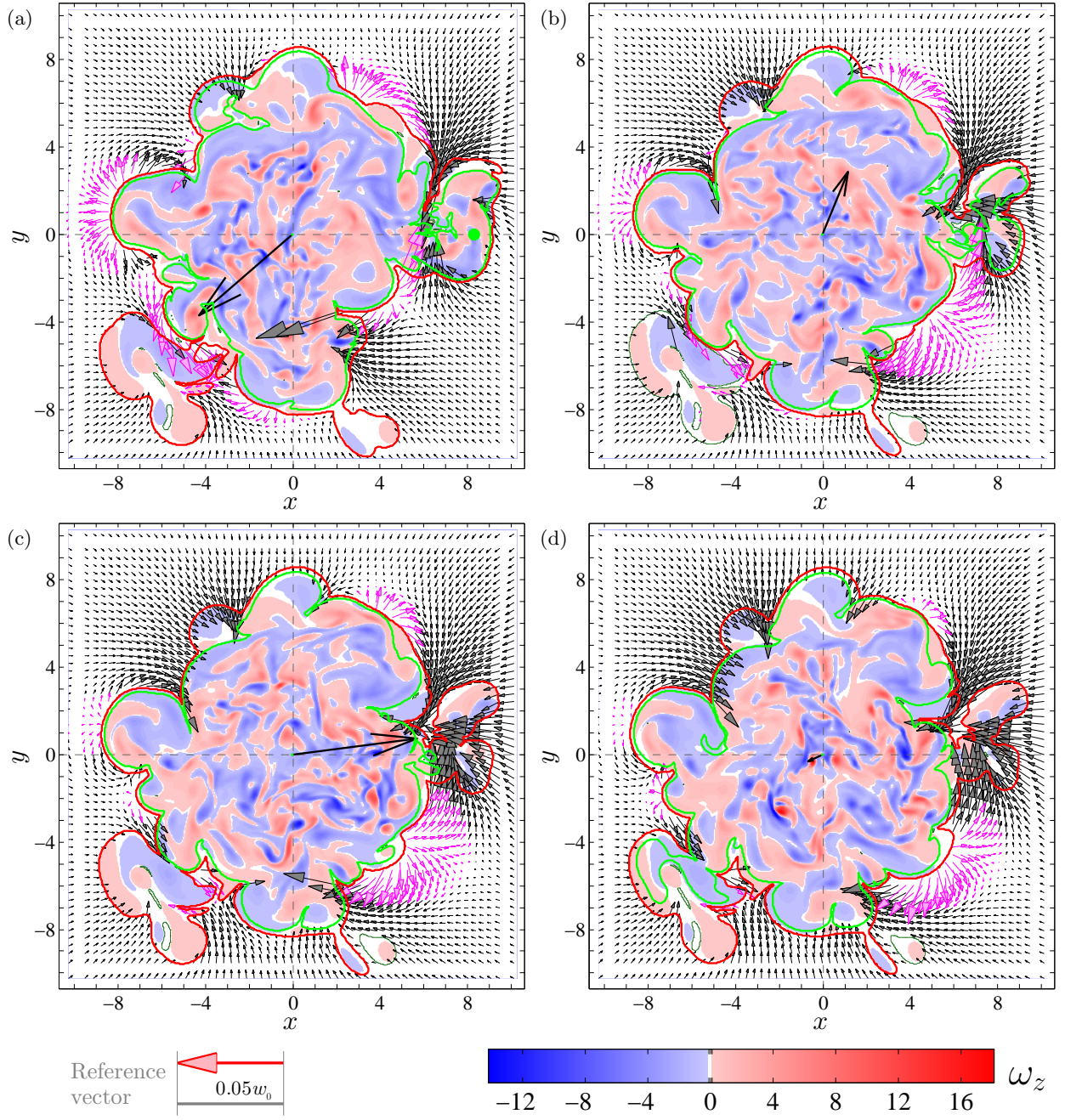


FIG. 9. Four instantaneous diametral sections at same z and t as in Fig. 8. The background vorticity field is the signed axial component ω_z . See Fig. 8 for additional details.

is confined to a $2 \times 5 \times 2$ ovoid.

It may be noted that the in-rush events, so conspicuous in the axial section shown in Fig. 2 and Fig. 6, are substantially weaker in the diametral section. This suggests that the major contribution to entrainment is made by the inward and upward velocity induced in the ambient fluid due to elements of azimuthal vorticity in the coherent structure in the core.

To understand the evolution of the flow events in the near ambient of the turbulent core, the flow region in the diametral plane shown in Fig. 8 is divided into 8 approximately equal semi-quadrants A to H in the xy plane, e.g. starting with A in the angular sector $0^\circ < \phi < 45^\circ$ around the origin $(x, y) = (0, 0)$ and going round anticlockwise to H in the sector $335^\circ < \phi < 360^\circ$. The flow shows some very interesting features as can be clearly seen in Figs. 8(a) to (d), and documented in Table I. The turbulent core is largest at $t = 950$ (Fig. 8(b)), consistent with the fact that the

widest part of the coherent structure, with its base SR4-SR9 containing a vortex ring, is passing through the plane $z = 42.69$ at the time.

VII. RELATION BETWEEN VORTICITY FIELD AT T/NT INTERFACE AND ITS NEAR-NEIGHBOURHOOD

In most of the previous work, the boundary between the turbulent core and the ambient fluid has been determined by thresholds on either scalar concentrations [10, 15, 20] or an out-of-plane vorticity component [39]. Boundaries defined by the former have often been the subject of controversy mainly because of the vast difference between the diffusivity of the scalar and viscosity. Furthermore, the evolution equation of the passive scalar and vorticity are fundamentally different due to the absence of the stretching-tilting term in the former. One could argue that the gradient of a passive scalar and vorticity are orthogonal to each other in the limit of very high Peclet and Reynolds number as was shown in a recent work by Patwardhan and Ramesh (2018) [40]. They show that scalar gradient surface tracks the vorticity field if the two were aligned initially. However, they also showed that in the regions with sharp gradients the gradient of passive scalar and vorticity are not orthogonal. We know that at the T/NT interface the velocity and scalar gradients are sharp and as a consequence a scalar cannot faithfully represent the turbulent flow field. So vorticity is fundamentally the more logical criterion to use, but to determine all three components of the vorticity vector experimentally is difficult. The 3D results from DNS studies can therefore provide valuable insights from data on the full vector ω .

We have shown here that the use of $|\omega|$ sheds much light on the subject. The contour $|\omega| = 0.5$ is close to the turbulent core of the jet, and is a good candidate for the threshold defining the inner edge of an interface and is consistent with the choice $\omega_y \simeq 0.5$ made by Westerweel *et al.* (2009) [10] for the out-of-plane vorticity component (Ω_z in their notation). Thereafter $|\omega|$ drops steeply going outward; the $|\omega| = 0.5$ contour is approximately at the point where the outward gradient of $|\omega|$ is steepest in the T/NT interface (i.e., Corrsin's viscous superlayer), and is taken here as defining the inner boundary of the jet.

The nature of the irrotational flow in the ambient near the T/NT interface has not received enough attention. With the present simulation more precise pictures of the flow in the ambient have been constructed. These pictures show a considerable degree of organization or order in the flow, usually circulatory in nature but occasionally radial as well. It is often (but not always) possible to trace the circulatory motions as those associated with the presence of elements of organized large-scale vorticity in the turbulent core near the edge of the jet, making a highly plausible connection through the Biot-Savart relation. Given this connection, it is not surprising that the inner boundary of the jet, close to the region of transition from one structure to the next in the core flow, often shows sharp and intense incursions at velocities of order $0.4\bar{w}_c$ as already pointed out. The highest velocity in the outer field is $0.34\bar{w}_c$ at $x \approx 0.3$ and $z \approx 29.7$ in SR6 of Fig. 2. Axial sections of the flow show that along either inner boundary of the jet, about 4 or 5 'inrush events' of the above type and others (at an average streamwise spacing of 5) can be inferred. Although the length scale of a hypothetical 'lid' for such an incursion into the inner boundary covers only a small fraction of the surface area of the jet, the higher inrush velocities compensate to some extent for the lower area, and could contribute more significantly to the total entrainment than has been estimated in recent work (less than 8% according to Westerweel *et al.* (2009) [10]). The DNS images leave no doubt however that a significant part of the entrainment occurs through inrush events which have an episodic character, reminiscent of the momentum flux events that contribute to the Reynolds shear stress in a high Reynolds number atmospheric boundary layer (Narasimha *et al.* 2007 [1]).

In summary, these observations suggest the following physical picture.

1. The propagation - outward or inward - of the inner boundary, as well as the organized motion of the ambient fluid that rushes inward, can result in penetration that pushes inwards 'vulnerable' parts of the outer boundary. This process is encouraged by the Biot-Savart induced velocity in the ambient fluid due to elements of the vorticity field associated with the coherent structures in the core, leading to what has been called engulfment.
2. As long as there is a sharp boundary between turbulent and non-turbulent flow, entrainment into the core flow must involve fluid crossing a fractal inner T/NT boundary (which may itself be propagating into non-turbulent fluid); this could legitimately be called 'nibbling'.

It would be interesting to find out how the radial and axial components of velocity at the T/NT interface, which are primarily responsible for the fluid entrainment from the lateral and cross-sectional sides of a turbulent jet, are correlated to the relevant velocity components at the surfaces of a short circular cylinder circumscribing the T/NT interface. There is entrainment also in the axial or streamwise direction, *e.g.* just below S4-S9.

We first choose the radial components for analysis. Consider the diametral section at $z = 34.05$, in the middle of the self-preserving zone. We now choose a cylinder of height $6d_0$ ($32 \leq z \leq 38$), and a radius of $8d_0$ which is just adequate to lie close to but outside the T/NT interface almost everywhere around the circumference. Radial velocity vectors are plotted at both the T/NT interface and the cylinder circumference at the selected instant $t = 2050$ as shown in Fig. 10; vectors in magenta and green indicate respectively radially outward (generally detraining) and radially inward (generally entraining) velocities (neglecting the interface propagation velocity, see section IV). The contours within the T/NT interface show axial velocity.

The procedure for finding the correlations mentioned above (along with its limitations) is now outlined. The angular circumference of the disc (360 degrees, also periphery of the T/NT interface) is divided into 72 sectors, each subtending 5° at the center as shown in Fig. 10; this gives us enough sectors to make reliable estimates of the correlations.

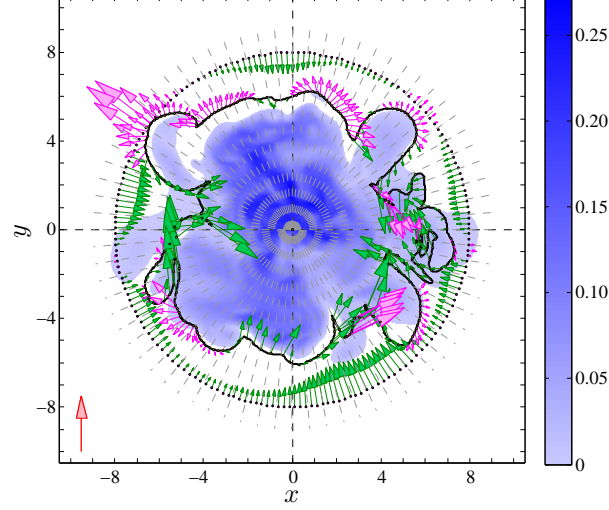


FIG. 10. Conventions followed for overlap analysis; see text for details. Diametral section at $z = 34.05$ and $t = 2050$ showing the contours of axial velocity and the velocity vectors at the T/NT interface and the cylinder circumference. The reference velocity vector shown in red at the bottom-left corner is $0.05w_0$. Velocity vectors at the disc circumference are scaled up by a factor of four relative to the vectors at the T/NT interface. Note that radially outward motions are rare and radially inward motions dominate.

We use the following conventions while calculating the correlation:

1. Correlated: If velocity vectors at both the T/NT interface and the cylinder are in the same direction, either inward or outward, then that event is said to be “correlated”.
2. Anti-correlated: If velocity vectors at the T/NT interface and the cylinder are in the opposite directions, either inward at the T/NT interface and outward at cylinder or vice versa, then that event is said to be “anti-correlated”.
3. Non-correlated / non-decisive: We classify the event as “non-correlated / non-decisive”
 - (i) if the velocities are negligibly small ($< 0.05w_c$). By inspection and trial, the threshold was determined to be about $0.001w_c$; for example, look at the sectors between 185° to 195° in Figure 10;
 - (ii) when it is difficult to decide about the correlation because the velocity at either T/NT interface or the outer circle is zero or very small ($\sim 0.001w_c$); for example, the velocity vectors at cylinder circumference in sector between 330° to 335° in Figure 11(a);
 - (iii) when the T/NT interface goes beyond the outer circle, which has been found to occur for three time instants viz. $t = 2100, 2125, 2150$ out of 8 time instants for less than about 40° in the total of 2880° studied, i.e., 1.4% of the circumference.
 - (iv) When the T/NT interface is highly convoluted, correlations are estimated using the velocity vectors at T/NT interface closest to the cylinder, and ignoring the inner T/NT interface. Figure 11(a) presents one such convoluted T/NT interface.

The eight time instants chosen for analysis are separated from their neighbours by 25 flow units adding upto a total duration of 200 flow units. We find that the velocity vectors are correlated for 73% of the circumference, anti-correlated for 24%, and non-correlated for 3%.

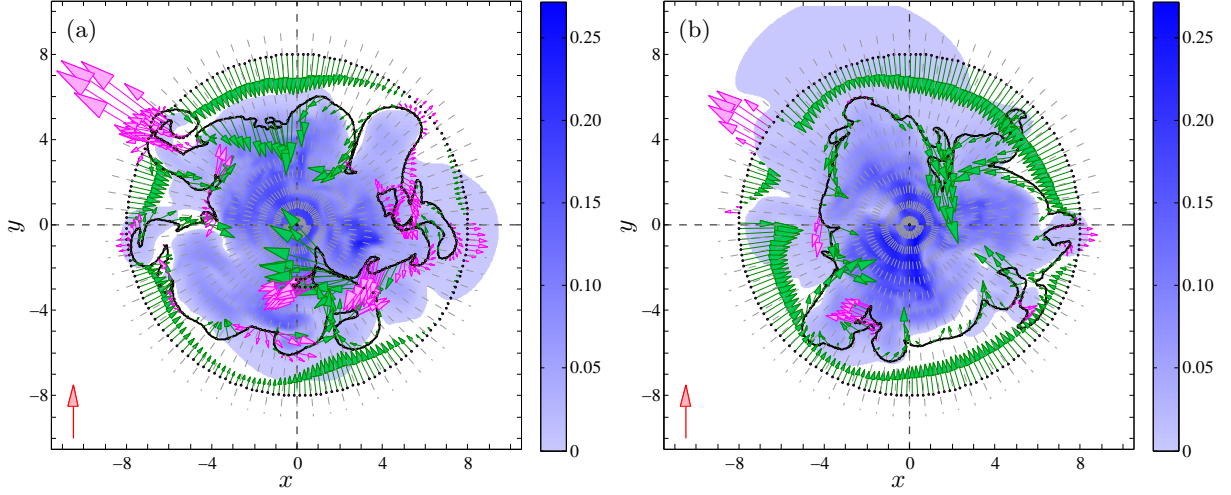


FIG. 11. See Fig. 10 for conventions. (a) Instantaneous image at $t = 2075$ indicating the difficulty in the selection of highly convoluted T/NT interface for finding the correlations, especially in the fourth quadrant. (b) An instantaneous event at $t = 2175$ showing strong entraining correlations between the radial velocity vectors at T/NT interface and cylinder circumference.

Figure 11(b) shows one instant when the velocity vectors at T/NT interface and cylinder circumference both inward and strongly correlated. Note that 65 out of 72 sectors (more than 90% of the circumference) are correlated and inward, while 7 out of 72 sectors are anti-correlated (i.e., less than 10% of the circumference). This suggests that entraining motions at the T/NT interface are strongly correlated with the radially inward component of the velocity at the cylinder's surface.

VIII. MASS FLUX BUDGET

This section presents the net mass flux budget within the turbulent core determined by $|\omega| = 0.5$ and also within the cylindrical disc at $t = 1995.25$ to demonstrate the accuracy of the mass flux entrainment calculations. This is done by calculating the streamwise variation of the mass flux in the turbulent core and correlating it with the mass flux entrained into a fixed cylindrical disc of radius $8d_0$ and height $\approx 6.5d_0$ circumscribing the T/NT interface. A schematic of the disc and the T/NT interface is shown in Fig. 12. The volume between the cylindrical disc surface and the T/NT interface will be called the sheath. The mass flux at the cylinder edge is computed as

$$\int \mathbf{u} \cdot d\mathbf{S} \quad (9)$$

where $d\mathbf{S}$ represents the local surface area vector at the edge of the cylinder. The mass flux in the turbulent core is computed using Eq. 9 where $d\mathbf{S}$ now represents the local area vector in the streamwise direction. The coordinates of the interface were detected with the iso-surface function in MATLAB using the criterion $|\omega| = 0.5$. The detected interface was mapped onto the nearest grid points in the computational domain, thus pixelising the interface. The advantage of this mapping is that the mass flux budget is accomplished to a very high accuracy as shown below and is not affected by any interpolation errors. The results are as follows:

Mass flux budget: cylindrical disc

Mass flux into the disc from the bottom surface ($m_{z_1=32.35}$) = 7.472

Mass outflux from the top surface of the disc ($m_{z_2=38.64}$) = 7.959

Mass flux into the disc from the lateral boundary (m_{NT_o}) = 0.486

Net mass flux into the disc accounting for surface normal= $m_{z_1} - m_{z_2} + m_{NT_o} \approx 10^{-11}$

Mass flux budget: turbulent core

Mass flux into the turbulent core from the bottom surface ($m_T(z_1 = 32.47)$) = 7.327

Mass outflux from the top surface of the turbulent core ($m_T(z_2 = 38.51)$) = 7.126

Mass outflux from the top sheath surface ($m_{NT}(z_2)$) = 0.798

Mass flux into the bottom sheath surface ($m_{NT}(z_1)$) = 0.155

Mass flux into the lateral boundary of the cylinder (m_{NT_o}) = 0.443

Total mass flux from the sides of the cylinder ($m_{NT_o} = m_T(z_1) - m_T(z_2) + m_{NT}(z_1) - m_{NT}(z_2)$) = 0.443

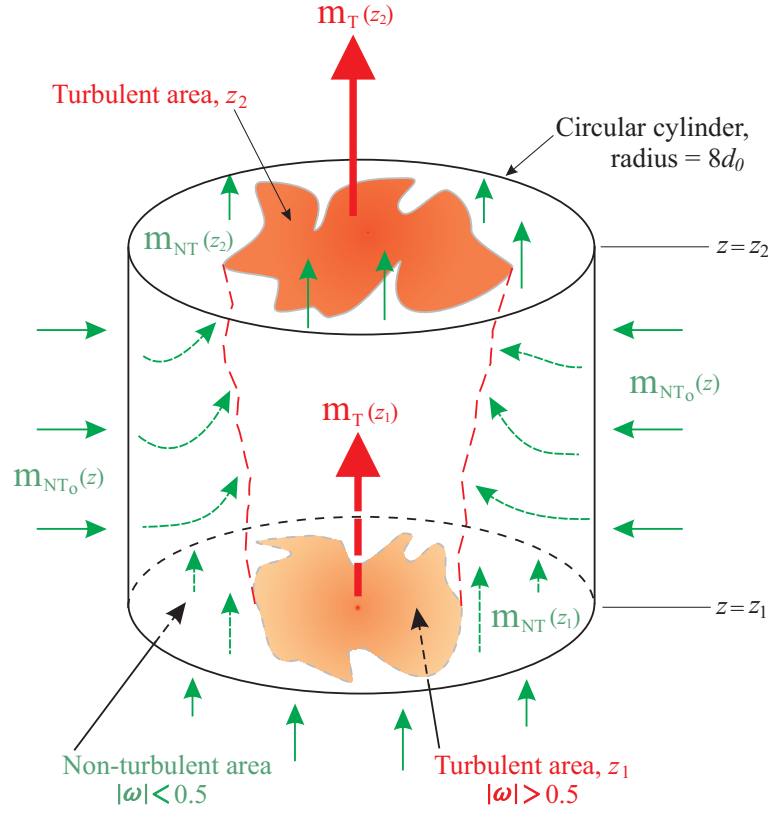


FIG. 12. Schematic for the mass flux budget (see text for details). Color code: red for turbulent motion (T), green for non-turbulent motion (NT).

$$\text{Mass flux balance} = m_{NT_0} - m_{NT_0^*} = 10^{-7}$$

It must be noted that the z location of the mass flux budget in the core and the cylinder is slightly different due to the staggered location of velocity and vorticity. This results in a slightly different mass flux from the lateral boundary of the cylinder. From the numbers given above it is seen that the entrainment mass flux calculations at the T/NT interface are accurate up to 10^{-7} and the continuity equation up to 10^{-11} . At $t = 1995.25$, for $32.5 \leq z \leq 38.5$, we note that the disc had a net mass flux entraining into the cylinder and the turbulent core had a net mass flux detraining from the core. This would seem to suggest that the dynamics at the T/NT interface and the cylinder are not in sync as opposed to the conclusion derived in the previous section. This may well be due to the fact that conclusions in the previous sections did not account for the magnitude of these events. However, it must be noted that the present inference is based on the analysis of a single time instant. A more detailed analysis is required to understand the entrainment dynamics close to the T/NT interface. We also compute the Taylor entrainment coefficient $\alpha_E = \frac{1}{2\pi W_c b_{we}} \frac{d\bar{m}}{dz}$ [41] using the data averaged over 1750 flow units where \bar{m} represents the mean mass flux within the turbulent core, W_c is the mean centreline velocity and b_{we} is the mean velocity width, defined by $w(b_{we}) = W_c/e$. The entrainment coefficient in the self-preserving region in the present data is 0.065 which is smaller than the $\alpha_E = 0.074$ at $z \approx 34$ reported in Carazzo *et al.* (2006) [42]. This was expected, as the present calculation does not account for the mass flux outside the turbulent core, in contrast to the analysis in Carazzo *et al.* (2006). Additional details are discussed in Shinde *et al.* (2019).

IX. ENTRAINMENT AS AN EPISODIC PROCESS

To study the nature of entrainment in a turbulent jet it is important to understand how the irrotational ambient fluid enters into the turbulent jet. Figure 13 shows the streamwise variation of the radial mass flux entering into the lateral surface of the $8d_0$ disc at various instants. We see that entrainment varies in both space and time, and it can be spatially anti-correlated in z . Thus, the net entrainment in the region $32 < z < 35$ at a given instant is anti-correlated with the net entrainment in $35 < z < 39$. Figure 14 shows the variation of streamwise mass flux in

the turbulent core, obtained by integrating the streamwise velocity over the area within the T/NT interface at any z . The anti-correlation observed at the edge of the cylinder is not as strongly visible in the streamwise mass flux data. Some of the mass flux entrained into the cylinder may be retained in the non-turbulent region outside T/NT interface. We note that the mass flux in the turbulent core of the jet increases between $34 \leq z \leq 38.5$ over the time span shown in Fig. 14. This is not surprising as it is linked to the passage of large scale coherent structures. The presence of these structures locally enhances entrainment events that explains the increase in the mass flux in the turbulent core. And in the absence of these structures the mass flux in the core decreases. The decrease in the mass flux in the core is visible in the region between $32.5 \leq z \leq 34$ for the duration $2030 \leq t \leq 2045$. This trend would propagate downstream at later times, and the cycle repeats. Similar observations were reported in the recent studies on turbulent plumes [20, 21]. To understand the nature of these observations it is necessary to examine the entrainment dynamics close to the T/NT interface.

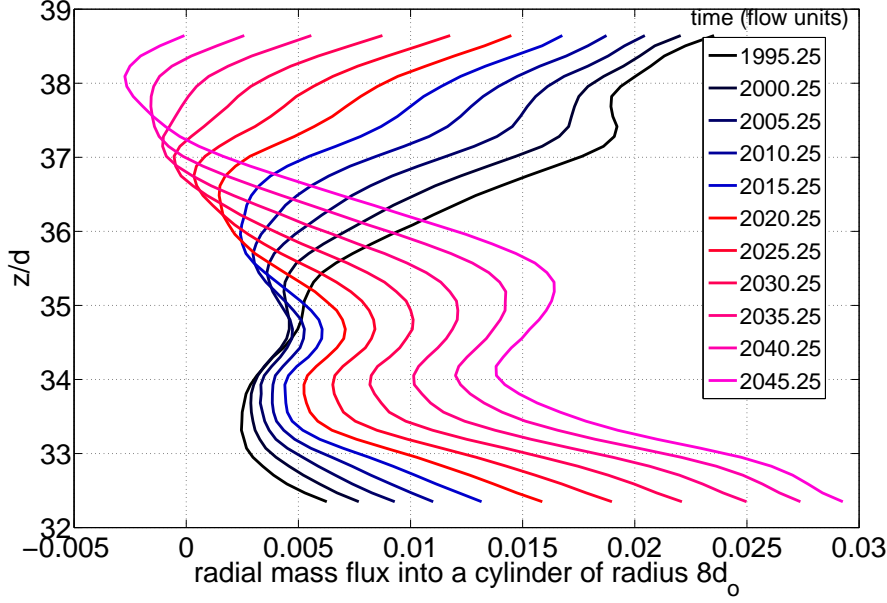


FIG. 13. Streamwise variation of radial mass flux into the $8d_0$ diameter cylindrical surface. Time indicated in flow units.

Figure 15 shows the azimuthal variation of mass flux at the R/IR interface at intervals of 2° . In certain angular regions there exist several interface co-ordinates due to the contortions in the interface. At these locations only the mass flux spatially averaged over 2° is plotted. Figure 15 shows that there are instances when localized regions of very high mass flux entraining into or detraining from the turbulent core. At such times, the mass flux contributions from the positive events are significantly larger than from the negative events. From Fig. 15 and earlier images (e.g., see Fig. 2) it appears that entrainment is episodic. We identify about 13 to 16 such events at each z location shown in Fig. 15. Some of these events or episodes may be spatially correlated. To better describe this episodic character we use the algorithm described by Narasimha *et al.* (2007) [1] where they adopted a threshold method to identify the productive and counter-productive periods in an atmospheric boundary layer momentum flux time series. Following their analysis we adopt the r.m.s. value m^* as an appropriate unit for the threshold, and an event is detected if the instantaneous mass flux $m(t, z, \phi)$

$$|m| > km^*, \quad (10)$$

where k is a constant to be selected. This is done by examination of the data at the T/NT interface at intervals of 2 degrees in the azimuthal angle (ϕ). The angular extent of an event in the azimuthal direction is defined as a continuous interval in the azimuthal angle where Eq. 10 holds true. This entire interval is then considered as one spatial event at a given instant.

We define a few additional parameters to characterize the events. The amplitude of an event i is defined as

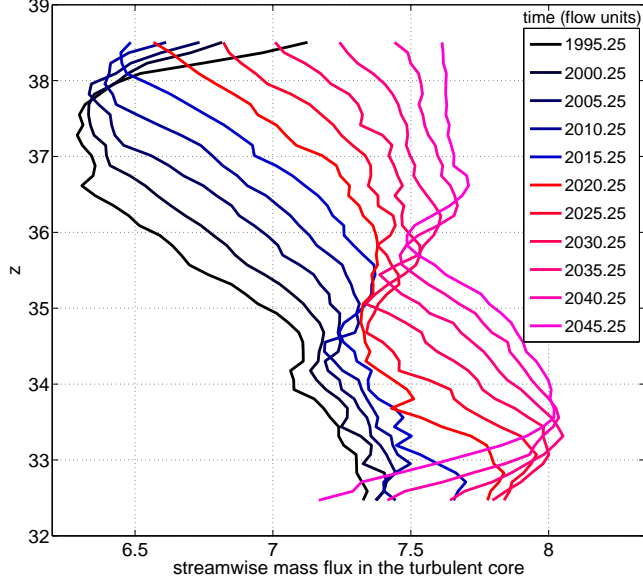


FIG. 14. Streamwise variation of the mass flux within the T/NT interface ($|\omega| = 0.5$). Time indicated in flow units.

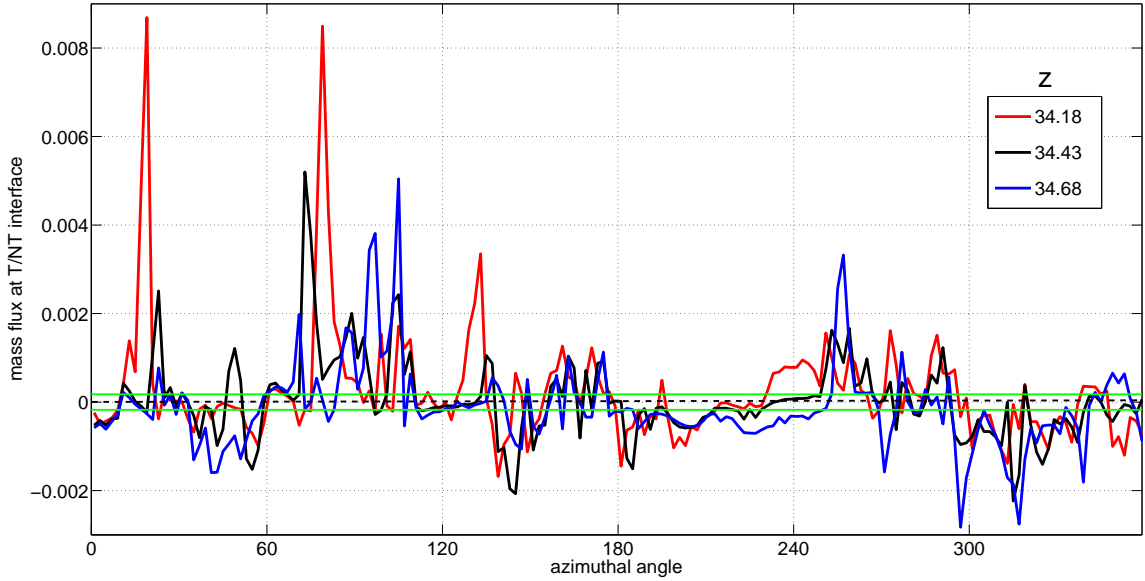


FIG. 15. Azimuthal variation of mass flux at the R/IR interface (threshold level on $|\omega| = 0.1$). The green lines indicate $\pm 30\%$ of *r.m.s* of the mass flux.

$$A_i(t) = \frac{1}{\overline{m}} \int_{\phi_{i1}}^{\phi_{i2}} \frac{m(t, z, \phi)}{\phi_{i2} - \phi_{i1}} d\phi, \quad (11)$$

where \overline{m} is the mean mass flux (averaged over time and space) across the T/NT interface and $\phi_{i2} - \phi_{i1}$ is the angular extent of event i . Thus the amplitude is the ratio of the contribution from an event to the mean value of the total net mass flux. The fractional mass flux contribution from an event i is given by

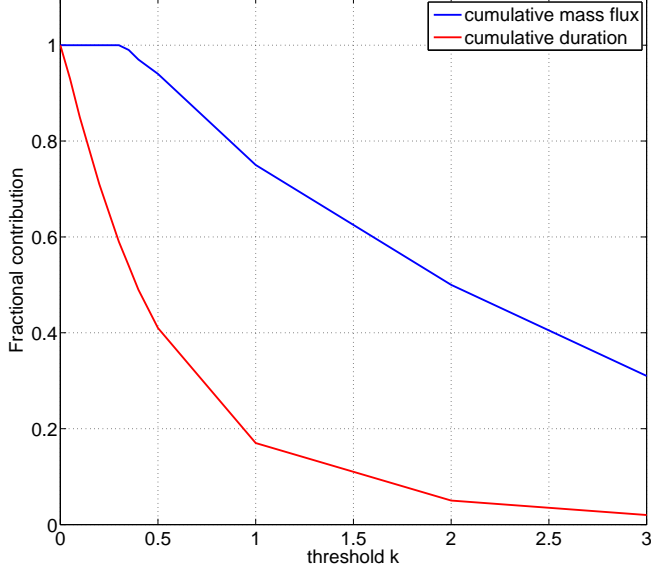


FIG. 16. Variation of fractional contribution to mass flux at the R/IR interface and the corresponding cumulative duration as a function of threshold k for event detection based on Eq. 10.

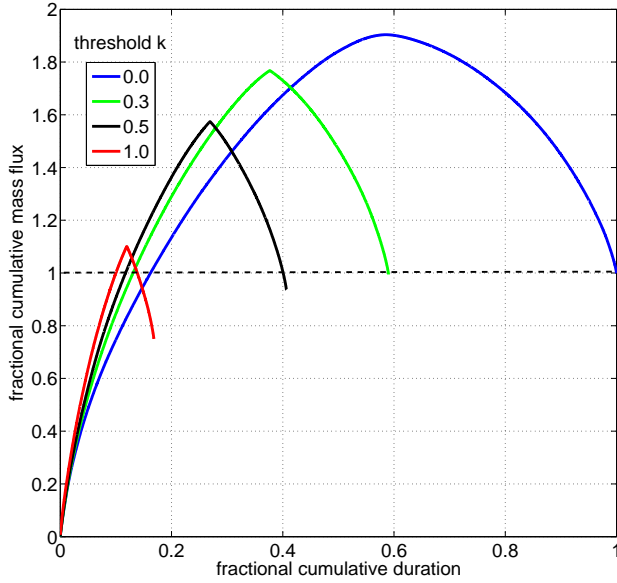


FIG. 17. Variation of cumulative mass flux as a function of cumulative duration for various event detection thresholds k . The events are arranged in descending order of the (signed) magnitude for calculating cumulative mass flux and cumulative duration.

$$m_i = A_i * \frac{\phi_{i2} - \phi_{i1}}{T}, \quad (12)$$

where T is the total length of the data set in degrees, over an appropriate number of realizations. So the net contribution of an event is a product of both amplitude and duration. Every event has a finite extent over time and

space. Note that the events are not tracked over time, only the azimuthal extent of the event at a given time is accounted for in the present analysis.

To determine the flux events the mass flux data at the R/IR interface were analyzed in $34 < z < 35$ for a total time of 185 flow units. In Fig. 16, the ratio of the cumulative contribution of detected events to the total mass flux for various values of the threshold is presented. The objective of this plot is to determine the appropriate threshold required to detect the minimum number of events that will account for almost the whole flux to describe the mass flux balance. From Fig. 16 such a threshold is around 0.3, as it accounts for about 99.5% of the total mass flux.

Narasimha *et al.* (2007) [1] also used a burstiness parameter to determine the compactness and significance of the detected events. The contribution from each event is calculated using eq. 12. The events are arranged in descending order of magnitude of their contributions from the largest positive through to the largest negative contribution. The cumulative contribution from this re-ordered sequence of events is then plotted against the cumulative duration of the events as shown in Fig. 17. The burstiness curve reaches a maximum when the contributions of all the entraining (positive) events have been integrated, and then decreases thereon due to the detraining (negative) events. The curve is plotted for various thresholds from 0.0 to 1.0. For a threshold greater than about 0.3, the detected events do not account for the total mass flux. This would suggest that for higher thresholds the weaker events are required for a complete description of the interfacial dynamics. For thresholds less than 0.3, contributions from sub-threshold events are like noise with zero mean with little net contribution to the net mean mass flux \overline{m} . For the threshold of 0.3, the total contribution from positive events reaches about $1.77\overline{m}$ over 37% of the total duration, and that from the negative events is about $0.77\overline{m}$ over about 22% of the total duration. Following the terminology from Narasimha *et al.* the positive events are called productive and the negative events counter-productive. The rest of the time, over which the net contribution is negligible, is called the idle phase.

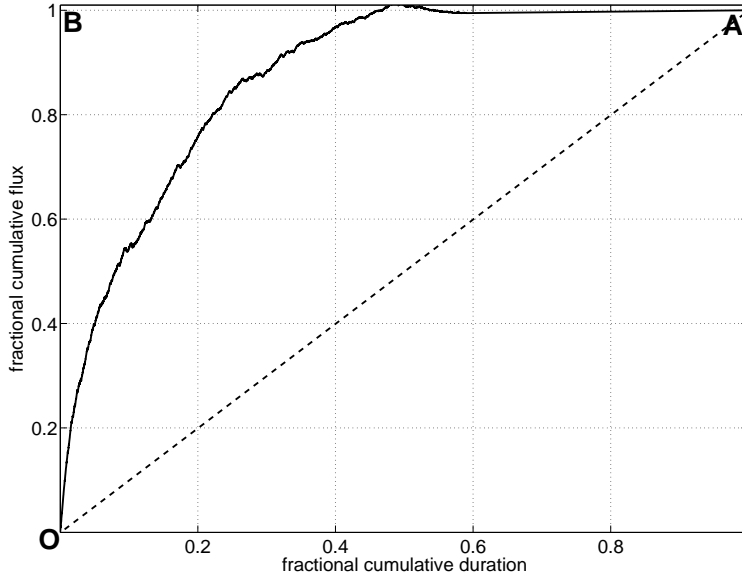


FIG. 18. Burstiness curve: Variation of cumulative mass flux as a function of cumulative duration for an event detection threshold k of 0.3. The events were ordered in the descending order of the absolute magnitude, for calculating the cumulative mass flux and the cumulative duration.

We may also choose to arrange the events ordered according to the absolute magnitude. With such an arrangement, the burstiness curve never exceeds unity and has small discontinuities, as shown in Fig. 18. Following Narasimha *et al.* (2007), the burstiness factor B is then defined as the ratio of the area between the curve and the line AO to the area of the triangle ABO. If $B = 0$ for an event series, then the burstiness curve is represented by the dashed line AO. This indicates that all events have equal contributions over equal durations for the entire dataset. On the other hand, if $B = 1$, then the burstiness curve would be the vertical axis BO, which implies that the events are like a series of delta functions with zero net duration, i.e. all the contributions occur instantaneously with zero duration with the amplitude approaching infinity such that the net contribution is finite. For the present data shown in Fig. 17, the burstiness factor is 0.75, which indicates that there are significant intermittent periods of intense activity at the R/IR interface that dictate the net mass flux entraining into the turbulent core.

The visual and quantitative analysis presented here so far suggests that the velocity field outside the T/NT interface is organized and are induced by the large scale ordered motions in the turbulent flow. The irrotational fluid is drawn towards the T/NT interface by the large scale coherent motions and not by viscosity-dominated nibbling. Moreover, the induced flow field could either be entraining or detraining depending on the organization and orientation of the vortices near the T/NT interface. The induced flow near the T/NT interface contorts the interface, and the irrotational fluid appears to be entraining into the turbulent core through spatially and temporally localized intense events wherein viscous action imparts vorticity to the irrotational fluid as it crosses the T/NT interface. Thus entrainment is a two step process. In the first step, which is also the rate limiting step, irrotational fluid is driven by the large-scale dynamics into the turbulent core through the gulf or well-like regions in the T/NT interface, and in the second step vorticity is imparted to fluid parcels through viscous processes as they cross the T/NT interface.

The two-step entrainment process discussed above is consistent with the views expressed by Plourde *et al.* (2008), Philip & Marusic (2012), Mistry *et al.* (2016) and Burrridge *et al.* (2017). Mistry *et al.* conclude that entrainment is a continuous multiscale process wherein at large scales the entrainment velocity is high to account for the smooth surface area and at smaller scales the entrainment velocity is relatively low, transporting flux occurring across a highly contorted fractal surface. Burrridge *et al.* analyse the data on plumes and highlight the influence of the large scale motions in the entrainment process through conditional statistics. They show that vertical mass transport is decreased or increased in the absence or presence of large scale eddies and conclude that these eddies impart significant vertical velocities to the ambient fluid near the T/NT interface. We relate it to motions induced by vortices in the coherent structures, especially the toroidal vortex at the base of the structure. Moreover, Burrridge *et al.* also show that the horizontal velocities are significantly enhanced in the absence of large scale eddies which in our analysis correspond to the region between the toroidal vortices of successive/neighbouring arrow head shaped coherent structures as in Fig. 2. The azimuthal variation of mass flux near the T/NT interface discussed in the present paper points to the episodic nature of entrainment. Further study will be required to determine whether all events may be associated with the large scale motions close to the T/NT interface and also to describe the shape of these events. It may be worthwhile to track the motions of the passive particles which originate from the irrotational region and study how they acquire vorticity near the T/NT interface.

X. CONCLUDING REMARKS

The objective of the present paper has been to describe the entrainment process in a round turbulent jet, using data provided by a well-resolved DNS study. As a preliminary step towards achieving this objective, detailed analyses of the DNS data have been made in the near-neighbourhood of the turbulent/non-turbulent (T/NT) interface, on the ambient as well as in the turbulent core neighbourhood of the interface. It is found necessary to distinguish a rotational / irrotational (R/IR) interface from the T/NT interface, the region in-between being rotational but not turbulent. Interestingly, it is found that the region between the core and the ambient have a length scale varying from the Kolmogorov to the Taylor length scales, indicating that both scales are relevant. The flow in the ambient neighbourhood of the T/NT interface is found to consist of several well-ordered circulating motions. By the analysis of such a flow field in a relatively simple case, wherein an approximately two-dimensional blob of vorticity is present, it has been shown that the ordered motion in the ambient flow is due to the induced velocity of vorticity elements in coherent structures in the core-side neighbourhood. When and where the ordered motions are relatively intense in the ambient, the T/NT interface is dented towards the core, which may develop into a deep and twisted well or gulf. It is shown that the entrainment process can be broadly divided into an engulfment phase near the edge of the jet, followed by nibbling across the T/NT interface deeper in the well, supporting a similar conclusion of Burrridge *et al.* (2017) regarding the episodic nature of the entrainment process. It is convenient to think of this process as constituting an entrainment event, intermittent in time and concentrated in space. These events are amenable to the method of analysis used for momentum flux events in the atmospheric boundary layer (Narasimha *et al.* (2007)). It is found that the burstiness of the signal is of the order of about 75%, with entrainment about 40% of the time, detrainment over about 10% of the time and very little activity over the rest of the time. This picture suggests that for applications where greater entrainment is desired, for example, one may have to devise means by which the intensity and duration of entrainment events can be enhanced.

[1] Roddam Narasimha, S Rudra Kumar, A Prabhu, and SV Kailas, “Turbulent flux events in a nearly neutral atmospheric boundary layer,” Philosophical Transactions of the Royal Society of London A: Mathematical, Physical and Engineering Sciences **365**, 841–858 (2007).

- [2] Stanley Corrsin and Alan L Kistler, *Free-stream boundaries of turbulent flows*, Tech. Rep. (NACA Report 1244, 1955).
- [3] Garry L Brown and Anatol Roshko, *Structure of the turbulent mixing layer*, Tech. Rep. (DTIC Document, 1972).
- [4] Garry L Brown and Anatol Roshko, "On density effects and large structure in turbulent mixing layers," *Journal of Fluid Mechanics* **64**, 775–816 (1974).
- [5] Paul E Dimotakis, Richard C Miake-Lye, and Dimitris A Papantoniou, "Structure and dynamics of round turbulent jets," *Physics of Fluids* **26**, 3185–3192 (1983).
- [6] Carlos B da Silva, Julian CR Hunt, Ian Eames, and Jerry Westerweel, "Interfacial layers between regions of different turbulence intensity," *Annual Review of Fluid Mechanics* **46**, 567–590 (2014).
- [7] J Westerweel, T Hofmann, C Fukushima, and J Hunt, "The turbulent/non-turbulent interface at the outer boundary of a self-similar turbulent jet," *Experiments in Fluids* **33**, 873–878 (2002).
- [8] David K Bisset, Julian CR Hunt, and Michael M Rogers, "The turbulent/non-turbulent interface bounding a far wake," *Journal of Fluid Mechanics* **451**, 383–410 (2002).
- [9] M Holzner and B Lüthi, "Laminar superlayer at the turbulence boundary," *Physical Review Letters* **106**, 134503 (2011).
- [10] J Westerweel, C Fukushima, Jakob Martin Pedersen, and JCR Hunt, "Momentum and scalar transport at the turbulent/non-turbulent interface of a jet," *Journal of Fluid Mechanics* **631**, 199–230 (2009).
- [11] Carlos B da Silva and Rodrigo R Taveira, "The thickness of the turbulent/nonturbulent interface is equal to the radius of the large vorticity structures near the edge of the shear layer," *Physics of Fluids* **22**, 121702 (2010).
- [12] M Wolf, B Lüthi, M Holzner, D Krug, W Kinzelbach, and A Tsinober, "Investigations on the local entrainment velocity in a turbulent jet," *Physics of Fluids* **24**, 105110 (2012).
- [13] Joseph Mathew and Amit J Basu, "Some characteristics of entrainment at a cylindrical turbulence boundary," *Physics of Fluids* (1994-present) **14**, 2065–2072 (2002).
- [14] Maarten van Reeuwijk and Markus Holzner, "The turbulence boundary of a temporal jet," *Journal of Fluid Mechanics* **739**, 254–275 (2014).
- [15] J Westerweel, C Fukushima, JM Pedersen, and JCR Hunt, "Mechanics of the turbulent-nonturbulent interface of a jet," *Physical review letters* **95**, 174501 (2005).
- [16] Jimmy Philip and Ivan Marusic, "Large-scale eddies and their role in entrainment in turbulent jets and wakes," *Physics of Fluids* **24**, 055108 (2012).
- [17] Dhiren Mistry, Jimmy Philip, James R Dawson, and Ivan Marusic, "Entrainment at multi-scales across the turbulent/non-turbulent interface in an axisymmetric jet," *Journal of Fluid Mechanics* **802**, 690–725 (2016).
- [18] JS Turner, "Turbulent entrainment: the development of the entrainment assumption, and its application to geophysical flows," *Journal of Fluid Mechanics* **173**, 431–471 (1986).
- [19] WJA Dahm and PE Dimotakis, "Measurements of entrainment and mixing in turbulent jets," *AIAA journal* **25**, 1216–1223 (1987).
- [20] H. C. Burridge, D. A. Parker, E. S. Kruger, J. L. Partridge, and P. F. Linden, "Conditional sampling of a high pcelt number turbulent plume and the implications for entrainment," *Journal of Fluid Mechanics* **823**, 2656 (2017).
- [21] Frédéric Plourde, Minh Vuong Pham, Son Doan Kim, and S Balachandar, "Direct numerical simulations of a rapidly expanding thermal plume: structure and entrainment interaction," *Journal of Fluid Mechanics* **604**, 99–123 (2008).
- [22] O M Phillips, "The irrotational motion outside a free turbulent boundary," in *Mathematical Proceedings of the Cambridge Philosophical Society*, Vol. 51 (Cambridge Univ Press, 1955) pp. 220–229.
- [23] P. Bradshaw, *Turbulence* (Sprindler-Verlag, Berlin, 1976).
- [24] Francis H Harlow, J Eddie Welch, *et al.*, "Numerical calculation of time-dependent viscous incompressible flow of fluid with free surface," *Physics of fluids* **8**, 2182 (1965).
- [25] RWCP Verstappen and AEP Veldman, "Symmetry-preserving discretization of turbulent flow," *Journal of Computational Physics* **187**, 343–368 (2003).
- [26] Prabhakaran Prasanth, *Direct Numerical Simulation of Transient Cumulus Cloud Flow*, Master's thesis, Jawaharlal Nehru Centre for Advanced Scientific Research, India (2014).
- [27] NR Panchapakesan and JL Lumley, "Turbulence measurements in axisymmetric jets of air and helium. part 1. air jet," *Journal of Fluid Mechanics* **246**, 197–223 (1993).
- [28] Christophe Bogey and Christophe Bailly, "Turbulence and energy budget in a self-preserving round jet: direct evaluation using large eddy simulation," *Journal of Fluid Mechanics* **627**, 129–160 (2009).
- [29] GN Taub, Hyungoo Lee, S Balachandar, and SA Sherif, "A direct numerical simulation study of higher order statistics in a turbulent round jet," *Physics of Fluids* **25**, 115102 (2013).
- [30] Sachin Shinde, Prabhakaran Prasanth, and Roddam Narasimha, "Turbulent jet: A dns study," EMU Scientific Report No. Jets19-1 (Jawaharlal Nehru Centre for Advanced Scientific Research, Bangalore) (2019).
- [31] M. G. Mungal and D. K. Hollingsworth, "Organized motion in a very high reynolds number jet," *Physics of Fluids A* **1**, 1615–1623 (1989).
- [32] AJ Basu and R Narasimha, "Direct numerical simulation of turbulent flows with cloud-like off-source heating," *Journal of Fluid Mechanics* **385**, 199–228 (1999).
- [33] R Narasimha, V Saxena, and S Kailas, "Coherent structures in plumes with and without off-source heating using wavelet analysis of flow imagery," *Experiments in fluids* **33**, 196–201 (2002).
- [34] Carlos Bettencourt da Silva and Ricardo José Nunes dos Reis, "The role of coherent vortices near the turbulent/non-turbulent interface in a planar jet," *Philosophical Transactions of the Royal Society of London A: Mathematical, Physical and Engineering Sciences* **369**, 738–753 (2011).

- [35] Carlos B da Silva and José CF Pereira, “Invariants of the velocity-gradient, rate-of-strain, and rate-of-rotation tensors across the turbulent/nonturbulent interface in jets,” *Physics of fluids* **20**, 055101 (2008).
- [36] JCR Hunt, I Eames, and J Westerweel, “Mechanics of inhomogeneous turbulence and interfacial layers,” *Journal of Fluid Mechanics* **554**, 499–519 (2006).
- [37] K R Sreenivasan and C Meneveau, “The fractal facets of turbulence,” *Journal of Fluid Mechanics* **173**, 357–386 (1986).
- [38] KR Sreenivasan, R Ramshankar, and Ch Meneveau, “Mixing, entrainment and fractal dimensions of surfaces in turbulent flows,” *Proc. R. Soc. Lond. A* **421**, 79–108 (1989).
- [39] Kapil Chauhan, Jimmy Philip, Charitha M de Silva, Nicholas Hutchins, and Ivan Marusic, “The turbulent/non-turbulent interface and entrainment in a boundary layer,” *Journal of Fluid Mechanics* **742**, 119–151 (2014).
- [40] S. S Patwardhan and O. N Ramesh, “Can vorticity in a fluid flow be tracked with a passive scalar?” personal communication (2018).
- [41] Taylor G. I., “Dynamics of a mass of hot gas rising in air.” LA Report 235 (US Atomic Energy Commission) (1945).
- [42] Guillaume Carazzo, Edouard Kaminski, and Stephen Tait, “The route to self-similarity in turbulent jets and plumes,” *Journal of Fluid Mechanics* **547**, 137–148 (2006).